A MOLECULAR DYNAMICS SIMULATION STUDY OF DYNAMIC PROCESS AND MESOSCOPIC STRUCTURE IN LIQUID MIXTURE SYSTEMS

by

Peng Yang

A dissertation submitted to the faculty of
The University of Utah
in partial fulfillment of the requirements for the degree of

Doctor of Philosophy

in

Physics

Department of Physics and Astronomy

The University of Utah

May 2015

The University of Utah Graduate School

STATEMENT OF DISSERTATION APPROVAL

The dissertation of **Peng Yang**

has been approved by the following supervisory committee members:

Yong-Shi Wu	, Chair	**9/18/2014** Date Approved
Feng Liu	, Member	**9/18/2014** Date Approved
Frank E. Harris	, Member	**9/18/2014** Date Approved
Stephan LeBohec	, Member	**9/18/2014** Date Approved
Valeria Molinero	, Member	**9/18/2014** Date Approved

and by **Carleton DeTar** , Chair/Dean of

the Department/College/School of **Physics and Astronomy**

and by David B. Kieda, Dean of The Graduate School.

ABSTRACT

The focus of this dissertation is the Molecular Dynamics (MD) simulation study of two different systems. In the first system, we study the dynamic process of graphene exfoliation, particularly graphene dispersion using ionic surfactants (Chapter 2). In the second system, we investigate the mesoscopic structure of binary solute/ionic liquid (IL) mixtures through the comparison between simulations and corresponding experiments (Chapter 3 and 4).

In the graphene exfoliation study, we consider two separation mechanisms: changing the interlayer distance and sliding away the relative distance of two single-layer graphene sheets. By calculating the energy barrier as a function of separation (interlayer or sliding-away) distance and performing sodium dodecyl sulfate (SDS) structure analysis around graphene surface in SDS surfactant/water + bilayer graphene mixture systems, we find that the sliding-away mechanism is the dominant, feasible separation process. In this process, the SDS-graphene interaction gradually replaces the graphene-graphene Van der Waals (VdW) interaction, and decreases the energy barrier until almost zero at critical SDS concentration. In solute/IL study, we investigate nonpolar (CS_2) and dipolar (CH_3CN) solute/IL mixture systems. MD simulation shows that at low concentrations, IL is nanosegregated into an ionic network and nonpolar domain. It is also found that CS_2 molecules tend to be localized into the nonpolar domain, while CH_3CN interacts with nonpolar domain as well as with the charged head groups in the ionic network because of its amphiphilicity. At high concentrations, CH_3CN molecules eventually disrupt the nanostructural organization.

This dissertation is organized in four chapters: (1) introduction to graphene, ionic liquids and the methodology of MD; (2) MD simulation of graphene exfoliation; (3) Nanostructural organization in acetonitrile/IL mixtures; (4) Nanostructural organization in carbon disulfide/IL mixtures; (5) Conclusions. Results of MD simulations of liquid mixture systems carried out in this research explain observed experiments and show the details of nanostructural organizations in small solute molecules/IL mixture. Additionally, the research successfully reveals the correct mechanism of graphene exfoliation process in liquid solution. (This will be summarized in Chapter 5.) The research presented in this dissertation enhances our understanding of the microscopic behaviors in complex liquid systems as well as the theoretical method to explore them.

CONTENTS

LIST OF FIGURES

LIST OF TABLES

ACKNOWLEDGMENTS

I would like to thank my supervisor Dr. Feng Liu, for giving me the support to finish my thesis work when I was at the bottom point of my PhD study. His high level of knowledge, rich experience of all kinds of simulation and great insight into the physics behind the problem are inspiring. Moreover, he is always there and ready to provide you with valuable help at any time. Besides that, he is also a good friend for everyone in the group, and I can't forget the beautiful times when our group members spent time together hiking in the mountains, barbecuing in his back yard and celebrating Chinese new year.

I also want to give thanks to my supervisory committee members, Dr. Yong-shi Wu, Dr. Valeria Molinero, Dr. Stephan LeBohec, Dr. Frank E. Harris and also my previous advisor Dr. Gregory A. Voth for teaching me the knowledge, helping me in the research and monitoring my progress. I appreciate their donation of time and energy very much.

I would like to thank my colleagues and friends for making my life wonderful and happy. Especially, I would like to thank our department secretary Jackie Hadley for giving me so much help when my wife and I first came to Utah, and Andrew Merrell, for kindly checking my English spelling and grammar in this dissertation.

Finally, I dedicate my dissertation to my whole family: my wife, my parents, my brother and my lovely son. My wife, who traveled so far from China to Utah, lives with me together, shares happiness and sadness, is supportive at any time. My parents, who sacrifice so much to support me for so many years and never ask for anything. Lastly, I would like to thank my brother and my son for making my life gorgeous.

CHAPTER 1

INTRODUCTION TO GRAPHENE, IONIC LIQUIDS AND MOLECULAR DYNAMICS SIMULATION

In this chapter, we will discuss two core materials and the methodology used in my research. The materials are graphene and IL. While at a first glance, these materials may seem very different, they share some common features such as good and diverse properties, and a promising wide range of applications, which makes them hot topics in both fundamental and applied research. Another common feature is that they both can be investigated by using classical MD simulation. This chapter is organized in the following order: we first introduce the background of graphene and review its current production methods. Next ILs are introduced and followed by a discussion of their physiochemical properties and applications. Finally, we discuss MD simulation (including its techniques and development) which is considered the state-of-the-art methodology in studying complex liquid systems (in this case dispersed graphene and solute/IL mixture). This chapter will help readers understand why the systems studied herein are important and how MD simulations can be carried out to explore these systems.

1.1 Introduction to Graphene

First, some introduction and background are given on graphene (Figure 1.1). Properties and potential applications are then discussed. Finally, the current development of graphene production methods are briefly reviewed.(These production methods directly relate to our graphene liquid exfoliation study in Chapter 2.)

1.1.1 Brief History of Graphene, Its Properties and Potential Applications

Graphene is a two-dimensional (2D), one-atom thick material made of *sp*-bonded carbon atoms which are packed into a honeycomb lattice [1,2]. It is the building block of fullerenes (zero-dimensional), carbon nanotube (one-dimensional), graphite (three-dimensional) and

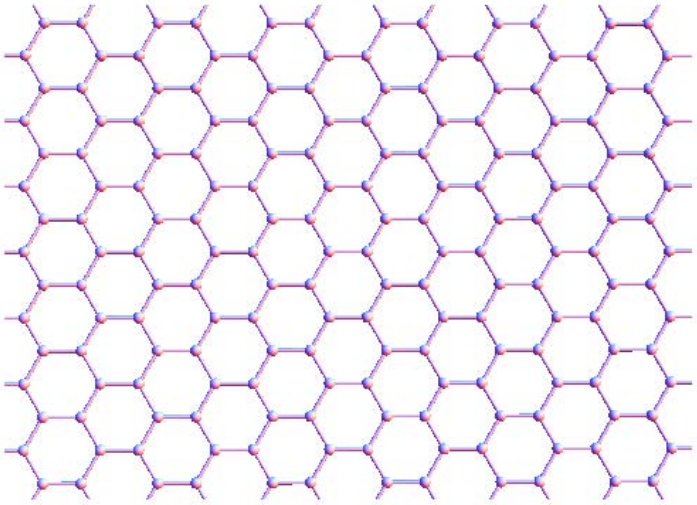

Figure 1.1. Graphene structure: honeycomb structure made of one layer thick carbon atoms.

some other carbon allotropes. Because of its unique atomic structure, graphene displays a lot of remarkable physical, chemical and mechanical properties [3] which make it a rising star material in both fundamental study and potential industrial application [4].

Graphene had been studied theoretically in 1947 by Wallace [5]. By using the tight binding approximation, he developed the electronic band structure of graphene and noted its linear dispersion. Followed by McClure, the diamagnetic susceptibility and energy level in a magnetic field had been calculated [6]. The effective mass and similarity to Dirac equations had been discussed by DeVincenzo and Mele [7]. Although the physical properties of this 2D crystal had been studied early on, it was believed that 2D crystals are thermodynamically unstable and cannot exist in the free standing state. It was a big surprise that in 2004 Geim and Novoselov successfully exfoliated few-atomic-layer, even monolayer thick graphite (i.e., graphene) and showed its structure.

Since then, graphene study has been the hot topic for both fundamental and applied research studies in the past decade. The electron mobility of graphene is remarkably high $\sim 2 \times 10^5$ $\mathrm{cm^2V^{-1}s^{-1}}$ [8,9] at room temperature, which is about two orders of magnitude higher than that of silicon transistors $\sim 1.4 \times 10^3$ $\mathrm{cm^2V^{-1}s^{-1}}$. This makes the observation of unusual quantum Hall effect [10-12] more convenient. The corresponding resistivity of the graphene sheet is $\sim 10^{-6}$ Ω-cm, less than the lowest resistivity of silver(Ag)$\sim 1.6 \times 10^{-6}$ Ω-cm. Mechanically, graphene is the strongest 2D material ever found, with high Young's modulus $\sim 1,000$ Gpa and intrinsic strength of 130 Gpa [13]. In optics, monolayer graphene absorbs 2.3% of white light, which makes it visible in vacuum [14]. Because of its unique properties, people pursue it as an excellent candidate in many applications, such as gapless analogue devices (frequency multiplier [15], zero-voltage detectors [16]), graphene membrane support [17], transparent conductor coating [18], graphene transistors [19,20], graphene composites [21], graphene photodetectors and photovoltaic cells [22].

1.1.2 Graphene Production Method

Graphene's superior properties have attracted a lot of attention [24-26]. However, many excellent characteristics are only observed in high-quality and very small samples. As a result, one of the bottlenecks of graphene applications is the mass production of graphene: we must produce a large quantity of high quality monolayer and few-layer graphene films at a relatively low cost. Currently, there are a number of graphene production methods that can be divided into two categories: top-down and bottom-up methods. Both of them are developing rapidly and each one has its own advantages and disadvantages. In the following part, we will discuss several popular methods.

The first discovered graphene in the world is a small piece of layer split from graphite (top-down approach) [1]. The whole process is quite simple: using a common adhesive tape, repeat the stick and peel process many times on a sample of graphite until there are a few layers of graphene flakes left, then transfer them to a chosen substrate by a gentle press of the tape. After removing the tape, some flakes (a few layers or sometimes a single layer) stay on the surface of the substrate and provide high quality graphene for further study. This is called micromechanical cleavage or "Scotch-tape" method. The key point is to find a suitable substrate that has appropriate VdW attraction with the graphene layers. This method is easy and cheap, no special equipment is required, no complicated processes are needed, and the graphene flakes produced in this way are pure and usually high quality. However, it suffers from several disadvantages. First, the graphene yield of this production process is extremely low and for a small micrometer sized graphene flake, one has to waste a large chunk of Highly Ordered Pyrolytic Graphite (HOPG). Therefore, it is a labor-intensive task, not suitable for large-scale mass production. Second, the graphene films produced by this method are uneven: the size and the thickness vary a lot, which may change the graphene properties. Third, the process is full of randomness and uncertainty, which cannot be scaled up for standard industry production procedure. Therefore, many other graphene synthesis methods have been developed in order to produce pure, even and cheap graphene films to benefit both fundamental and industrial research.

One often-used top-down graphene preparation method is graphene oxide reduction [27,28]. There are two steps involved: Step 1. synthesis of graphite oxide(GO); Step 2. reduction of GO. In step one, GO is synthesized by oxidation of graphite using some oxidants such as sulfuric acid, nitric acid, etc. Through oxidation, the oxygens and hydroxyl groups have been introduced into graphite; that makes GO highly hydrophilic and easily dispersed in water solution. After the treatments of ultrasonication and centrifugation, a stable homogeneous colloidal suspension is obtained, which includes very thin or even monolayer flakes of GO. Then chemical reduction is performed on theses flakes to produce graphene. Since the reduction can only be done partially, the intrinsic electronic structure of graphene has been disrupted by residual hydroxyl groups. As a result, a lot of defects and disorder form. Therefore, the product is often of low quality, e.g., electrically insulating, lower conductivity compared with pure graphene. Later, an even simpler solution-based exfoliation without any chemical reaction has been proposed and has achieved certain success [29-32]. In this method, graphite powder is directly dispersed into some organic solvents or surfactants/water solutions, then solvent molecules gradually attach to the

surface of graphene through repeated exfoliation and purification process. This dispersed graphene is defect free, lasts for a long time and usually yields well. Because of the surface energy match between graphene and solvents, the separated graphene flakes are stable and do not re-stack to form graphite. Coleman's group even pushed further in this liquid exfoliation direction. They eliminated the step of ultrasonication, by using high shear rate, and improved the graphene production rate up to hundreds of liters in liquid volume [33], which makes the production of graphene easily scalable up to the industry standard. Recently, this method has also been extended to exfoliate other 2D materials successfully [34,35]. The detailed simulation study of this liquid exfoliation of graphene is in Chapter 2. Another top-down method is graphite intercalation compound [36]. By inserting atoms or molecules into graphite, VdW interaction between layers is greatly reduced. This intercalation compound can then be dispersed into some organic solvents, and hence leads to complete dissociation of graphene layers.

In the category of bottom-up methods, chemical vapor deposition (CVD) is the most promising one which has been widely studied now [37]. Large-area graphene films can be grown on metal substrates, such as nickel and copper. The graphene films produced by this method show equivalent transport properties of those from micromechanical cleavage. The process can be controlled to form single-layer, bilayer or multilayer graphenes, and these films have been successfully transfered to other substrates. Although this method has achieved certain success, it still suffers from defects, grain size and nonuniform film thickness. In addition, transfer process and energy cost issues have to be considered before this technology become commercially available.

Other well-known graphene growth methods such as epitaxial growth on silicon carbide (bottom-up) [38,39] have also been used to produce large-scale, high-quality graphene films. The main problems of this production are high temperature processing, difficult morphology control and high cost.

1.2 Ionic Liquids (ILs)

Another material we are interested in is IL. We briefly discuss its concept, properties and current applications. The detailed study of IL mixture systems can be found in Chapter 3 and 4.

1.2.1 Introduction to Ionic Liquids

Ionic liquids, sometimes called room temperature ionic liquids (RTILs), are organic salts in liquid state. Unlike ordinary liquids such as water, which are made of electronically

neutral molecules, ILs consist of ions and ion pairs (Figure 1.2). ILs usually have melting points below some arbitrary temperature, for example 100 °C or as low as room temperature, which makes them different from traditional molten salts with a high melting temperature. Therefore, ILs offer an opportunity to conduct some experiments at low temperatures that were previously only feasible at high temperatures. Apart from being liquids at room temperature, ILs exhibit many other unique properties [40-44], such as low volatility, negligible vapor pressure, moderate electrical conductivity, excellent thermal stability, tunable viscosity, good heat capacity, miscibility with water, including both organic and inorganic ions, and a wide electrochemical window. The melting temperature and the range of liquid state vary with different combinations of cations and anions. Nowadays, the estimated number of ILs is on the order of 10^{18} [45], and about several hundreds of ILs are already commercially available for particular applications. As such a big family with good and diverse characteristics, much attention has been paid to ILs of its properties and potential applications.

1.2.2 Physicochemical Properties of Ionic Liquids

The physical-chemical properties of ILs are determined by the structure and properties of its constituent cations and anions.

Melting point is an important characteristic for ILs; it is closely related to the structure and intermolecular interaction. It is well known that a low-symmetry cation often leads to a low melting point of an IL. For example, the melting point of imidazolium-based ILs decreases with the increasing length of alkyl chain on the imidazolium ring [45]. Also, a weaker intermolecular interaction such as delocalization of electrons also contributes to a lower melting point [45,46]. Therefore, selection of various cations and anions can control the melting point of an IL.

Viscosity is another important factor which affects the applications of ILs, which is also associated with the structure of an IL. For pure ILs, viscosity is much higher than that of water or aqueous solution. The relatively high viscosity affects diffusion of solutes and causes practical problems when using ILs as media to conduct chemical reactions. Chemists have found that anion plays an more important role on viscosity than cation does. For the same cation, the $[NTf_2]^-$ anion often offers the lowest viscosity while the $[PF_6]^-$ contributes to higher viscosity [43-47]. For some ILs, the length of the side alkyl chain also affects the viscosity; a longer side chain usually means a higher viscosity [46]. Another factor that needs to be considered is the sensitivity to small amounts of impurity contamination [46]. Addition of a small amount of cosolvents may either increase or decrease the viscosity of

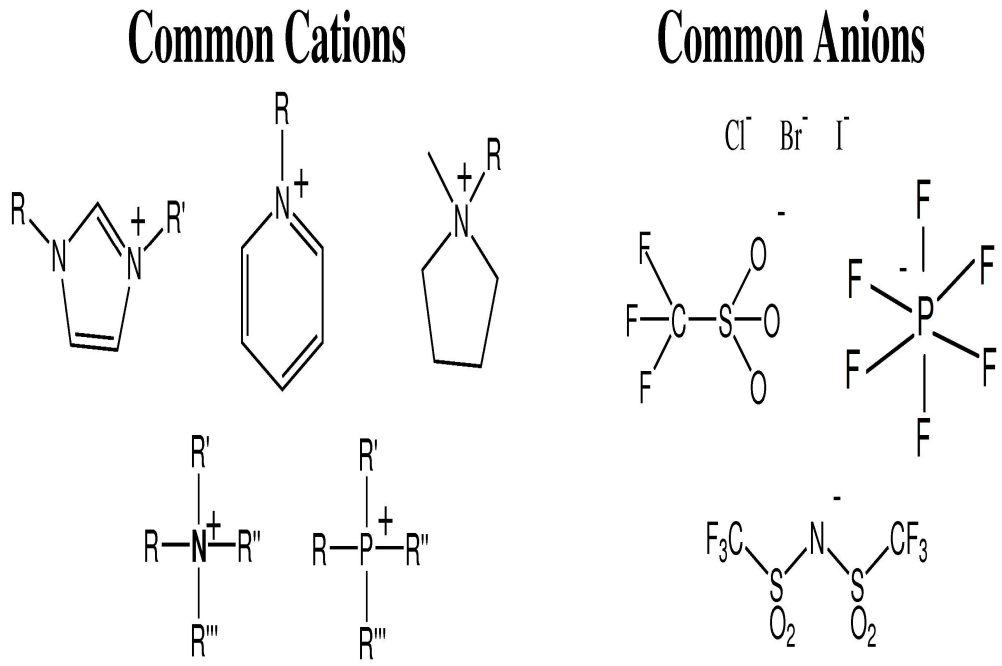

Figure 1.2. Some common cations and anions of ILs. R, R′,R″ and R‴ represent alkyl groups with arbitrary numbers of carbon atoms

air- or water-stable ILs; therefore, extraordinary care must be paid to handling this class of ILs. Other factors such as temperature, hydrogen-bonding ability also cannot be ignored in electrochemistry and synthesis.

Density and molar volumes are also important physicochemical properties that are affected by using different cations and anions, such as the length of the cation side chain. More detailed information can be found in some references [43,45].

1.2.3 Applications of Ionic Liquids

In synthetic chemistry, ILs provide a large number of useful solvents for carrying out chemical synthesis. The advantages of ILs as potential solvents can be summarized as the following: (1) They can dissolve both organic and inorganic materials, thus creating a good condition for many of chemical reactions. (2) They are nonvolatile, and therefore can be used in high vacuum systems to eliminate the contamination problem. (3) ILs are usually polar, noncoordinating solvents because of poor coordinating ions. Making battery electrolytes is another important application promised by the conductivity of ILs. However, stability, electrochemical window as well as polarity, dielectric constant and diffusion constant all need to be considered in the application of electrochemical devices. Other applications include biocatalysis, dispersing agents, gas handling, chemistry analysis, coatings, lubricant, liquid extraction [48].

Currently, many ILs can be produced by systematically synthesizing different combinations of cations and anions. Therefore, viscosity, melting point, dielectric constant and other physiochemical properties can be tuned. The search for low-melting points, low viscosity, high electronic conductivity, low toxicity, environment-friendly ILs will benefit both fundamental research and industrial application.

1.3 Molecular Dynamics Simulation

In the above two sections, we have introduced two materials (graphene and IL). Here we discuss the background, common techniques and current development of MD simulation. This dissertation will elucidate the details of the dissertation study which is the application of MD simulation in liquid mixture systems (dispersed graphene and solute/IL).

1.3.1 Role of Molecular Dynamics Simulation

Computer simulation is one of the powerful theoretical tools to investigate the properties of complex systems made of particles (molecules or atoms). By using numerical methods to solve the mathematical model of a N-body system (N>= 3) on the computer, it can explore

and gain new insights into material properties. Therefore, computer simulation has greatly enhanced our understanding of assemblies of particles which are too complex for analytical solutions. It also serves to explain experimental results, and make predictions to guide new experiments.

Computer simulation often acts as a bridge connecting theory with experiment (see Figure 1.3). We can test the theory by performing the simulation using the simplified mathematical model derived from the model system and compare simulated results to theoretical prediction. We can also carry out simulation and compare its results to experimental measurements to verify and improve the model. Through comparison, we can either modify the model and correct the theory or guide new experiments and make new predictions. There are two main categories of computer simulation: one is molecular dynamics, the other is Monte Carlo (MC) [49,50]. MC is a stochastic simulation that will not be discussed here. However, as a deterministic simulation, MD can investigate not only equilibrium but also transport properties. MD simulation solves the time dependent behavior of a molecular (atomic) system. After sufficiently long MD running, we can convert the microscopic information to macroscopic physical quantities by using the knowledge of statistical mechanics. MD simulation can provide detailed molecular (atomic) information of a material system and has been widely applied to investigate the structure, dynamics and thermodynamics of complex systems such as fluids, biological molecules, polymers, solid state crystals, defects, surfaces, clusters and fracture [51] .

1.3.2 Statistical Mechanics

Statistical mechanics is a branch of theoretical physics that studies the properties of a macroscopic system through consideration of its microscopic molecules (atoms). The goal of statistical mechanics is to understand macroscopic phenomena from the properties of its individual molecules instead of doing actual measurement. Statistical mechanics provides us with a method to connect microscopic averages with macroscopic observables such as pressure, volume, entropy and temperature. It starts with a hypothesis that the behavior of the system containing a large number of particles follows a certain probability distribution, by calculating the statistical average, thermodynamical observables of the system can be obtained.

In statistical mechanics, average values are defined as ensemble averages, which are given by the expression:

$$\langle A \rangle_{ensemble} = \iint A(p^N, q^N)\rho(p^N, q^N)\mathrm{d}p^N\mathrm{d}q^N \qquad (1.3.2.1)$$

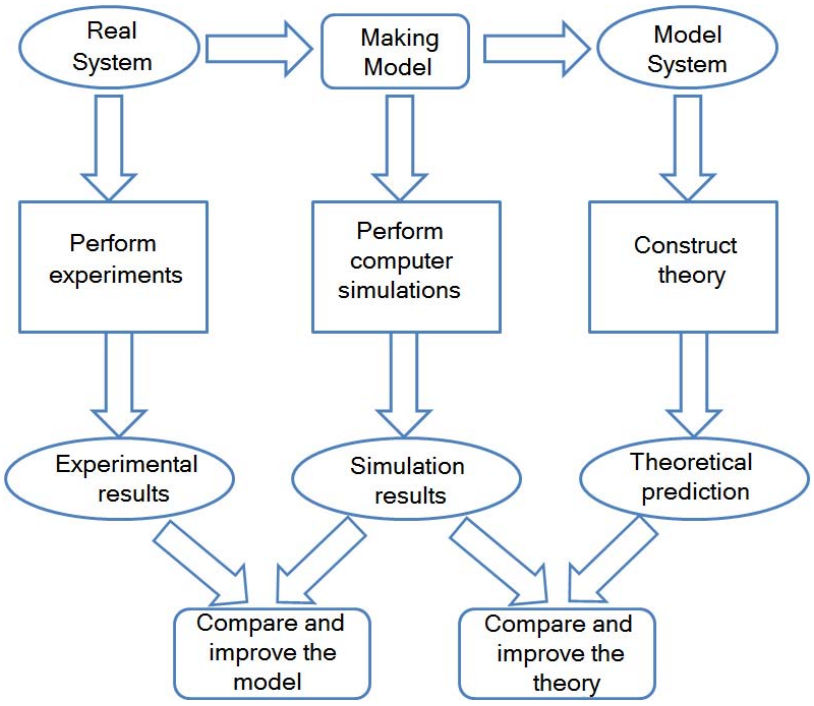

Figure 1.3. The role of computer simulation is as a bridge between experiment and theory.

$A(p^N, q^N)$ is the observable of interest, which is a function of momentum p and position q. p and q can be considered as coordinates in a multidimensional space called phase space (p^N, q^N). N means that there are N particles; therefore, the phase space has 6N dimensions. A microscopic state is just one point of the phase space. An ensemble is a collection of all the possible microscopic states satisfying certain conditions and representing a single macroscopic state. The integration is over all possible states of the specific ensemble. The most widely studied ones are microcanonical, canonical and grandcanonical ensembles. The details about the definitions, the partition function and derivation of ensemble averages can be found in any standard college level statistical mechanics textbook.

Generally, the probability density function in canonical ensemble can be written as the following expression:

$$\rho(p^N, q^N) = \frac{1}{Q} \exp\left(\frac{-H(p^N, q^N)}{k_B T}\right) \tag{1.3.2.2}$$

$H(p^N, q^N)$ is the Hamiltonian, T is the temperature, k_B is Boltzmann constant. Q is the partition function that is expressed in the following equation:

$$Q(p^N, q^N) = \iint \exp\left(\frac{-H(p^N, q^N)}{k_B T}\right) \mathrm{d}p^N \mathrm{d}q^N \tag{1.3.2.3}$$

Again, the integration is over all the possible states. However, it is extremely difficult to integrate them for a real system in which the particles interact with each other. In molecular dynamics simulation, the system passes through the possible states with the time evolution, so calculating averages in MD is given as the time average:

$$\langle A \rangle_{time} = \frac{1}{\tau} \int_0^\tau A(p^N, q^N) \mathrm{d}t \tag{1.3.2.4}$$

Ergodic theorem: after a long enough time, the system will go through all the possible microscopic states in the ensemble. Therefore, we can get the following equation:

$$\langle A \rangle_{ensemble} = \langle A \rangle_{time} = \lim_{\tau \to \infty} \frac{1}{\tau} \int_0^\tau A(p^N, q^N) \mathrm{d}t \tag{1.3.2.5}$$

This requires that a MD simulation has to run infinitely to calculate the time average which is equivalent to the ensemble average. In fact, a actual long MD simulation is always done for a limited time, so the calculated averages are only the approximate values of those macroscopic observables.

1.3.3 Classical Mechanics

Classical mechanics, as a branch of physics, investigates the properties of individual particles in the system. The core part is Newton's second law. For the motion of each particle, we can write the following equation:

$$m_i a_i = F_i \tag{1.3.3.1}$$

where m_i is the mass of the particle i, a_i is the acceleration of particle i, and F_i is the force exerted on particle i by other particles. This equation can also be written as:

$$m_i \frac{d^2 r_i}{dt^2} = F_i \tag{1.3.3.2}$$

Since the force is the gradient of the potential energy, it can be written as:

$$F_i = -\nabla V \tag{1.3.3.3}$$

V is the potential energy of the system and it is a function of positions of the particles usually. Combining (1.3.3.2) and (1.3.3.3), equation of motion of individual particle i can be expressed:

$$m_i \frac{d^2 r_i}{dt^2} = -\nabla V \tag{1.3.3.4}$$

So the total equations of motion for particle i are given:

$$\begin{aligned} \frac{dv_i}{dt} &= -\frac{1}{m}\nabla V \\ \frac{dr_i}{dt} &= v_i \end{aligned} \tag{1.3.3.5}$$

The equations of motion are deterministic. Once we know the initial positions and distribution of velocities, we can integrate equations (1.3.3.5) over time to get the trajectories of all the particles. Finally, all the thermodynamics quantities can be obtained by calculating the time averages in MD simulation.

1.3.4 Techniques of Carrying Out Molecular Dynamics Simulations

Based on the above discussion, we know that the essential part of performing MD simulation is to integrate the motions of equations (1.3.3.5), and a lot of methods have been developed, such as the leapfrog method, the velocity Verlet method and the Predictor-Corrector method [52]. Each one has its advantages and disadvantages. Therefore it is difficult to decide which one is the best to use at first sight. Often a lot of factors have to be taken into account for a specific MD simulation. First of all, one must consider the

energy conservation problem for a long term simulation to avoid a big accumulated error. Efficiency, accuracy and other problems are also important for a successful MD simulation. A good method for one problem is not necessarily good for another one, and an interested reader can read more about this in some classical reference books [53-55].

Another key point for doing MD simulation is the determination of potential energy, also called force field in classical MD simulation of biochemistry. The empirical potentials including both intramolecular and intermolecular interactions are usually calibrated to first-principle calculations of small model molecules and experimental results. These potentials are good for producing physical properties of systems which are at equilibrium or with small perturbations. They are not appropriate to study chemical reactions in which bonds break and form. This is always a problem of these force fields: their transferability. In is important to remember that the chemical environments of elements in model molecules are not the same of those in the system people are interested in when doing simulations, sometimes, even totally different. As a result, one force field cannot be applied to all the simulations; they have to be fit in some particular applications. That is the reason why there exist many force fields such as Amber, OPLS, CHARM, GROMAS etc., because they have different foci. Bond order potential is a popular choice of force field; it is designed to describe the different bonding states of an atom according to its environment such as number of bonds, bonding orientation and length. The well-known bond order potentials include the Tersoff potential [56], the Brenner potential [57] and the REBO potential [58]. Developing potential energy for MD simulation is still an intense and active area. Some other techniques (e.g., using periodic boundary condition to simulate bulk system and using Ewald summation to deal with long-range electrostatic interaction) are also important considerations.

1.3.5 Limitations

MD simulation has achieved certain success in predicting the macroscopic phenomena by doing computer experiments instead of doing exact experiment. However, it still suffers from some limitations [51].

1. Quantum effect. One of the backgrounds of MD simulation is classical mechanics, which is a good approximation when there are no electron transfer, proton tunneling, or chemical reactions. In chemistry and biochemistry, a large amount of very important processes such as photosynthesis, catalysis and charge transfer all involve quantum effects, which cannot be studied by traditional force field methods. In these cases, quantum mechanics is necessary to describe the characteristics of these processes, which leads to the development of first-principle/ab initio MD. In quantum MD simulation frame, the motions

of electrons and nuclei are separated. Electrons are small, light and fast-moving particles that need the treatment of quantum mechanics. Since nuclei are big, heavy and move slowly, classical mechanics is very accurate in studying their motions. However, quantum mechanics calculation currently based on Density Functional Theory (DFT) is only accurate for ground state electron properties, but less reliable to study excited state properties.

2. Time and size effect. The number of atoms of a systems that can be studied by using MD simulation now varies from a few thousands to about millions, and the total simulation time ranges from a few femtoseconds to milliseconds. MD simulation is about solving many-body interaction problems that are highly nonlinear, and the accumulated error will diverge with time evolution. When choosing an MD system size, the simulation cell length cannot be smaller than the spatial correlation length of the relevant quantities. Of course, an excessive big simulation cell that requires too much computation is not a reasonable choice. To save time, controlling accumulated error as well as representing relaxation time of interested physical quantities are both important in an MD simulation.

1.3.6 Advances of Molecular Dynamics Simulation

Recently, the most important advance of MD is so called multiscale modeling and simulation (Figure 1.4). It is the extension of MD in order to solve physical complex problems which have important characteristics in several different scales. It is based on recent development of computer techniques and improvement of algorithms. By applying different theories at different levels and incorporating them together, multiscale simulation uses numeric methods to solve many body problems and thus can help us understand phenomena from equilibrium to nonequilibrium properties, from structure to function, from microworld to macroworld. In a typical biochemical process such as enzyme reaction that often happens in solutions, the core chemical reaction is a fast quantum phenomenon that involves charge transfer. The reaction follows by the classical behavior of relaxation, and the whole molecular system is embedded in a dielectric continuum environment. In the core part of the reaction, quantum theory is appropriate for only a few to dozens of atoms, and then the marcomolecule made up of thousands of atoms can be described using classical mechanics, and the environment can be studied using a continuum model. These three different level theories in conjunction with each other, which have been realized in one simulation, can provide us with a complete dynamic picture of the phenomena, and hence deepen our understanding.

In many multiscale modeling and simulation techniques, the most famous technique is the coarse-grained (CG) model [59]. CG model, a method to fill the gap between

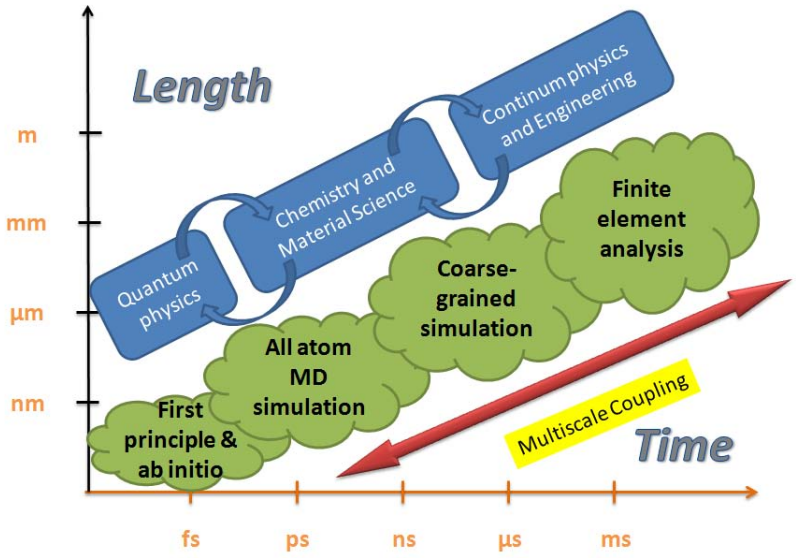

Figure 1.4. A schematic graph of multiscale modeling and simulation.

classical MD simulations and continuum model, makes the simulation and experimental results comparable. Currently, most of the MD simulations are still restricted to system size about a few nanometers and simulation length about dozens of nanoseconds due to available computer resources, which makes it very hard to directly compare computational results to experiment. CG is a computational technique developed to resolve this problem. The idea of CG is to reduce the degrees of freedom in a large system, and ignore the fine interaction details. In CG, several relevant atoms are treated as one group and represented by just one residue, the new system becomes a small one full of residues. As a result, the computation of a CG system needs fewer resources compared to the original all-atom one, and increased length and time scale of a large system can be simulated with a reasonable expense. One needs to remember that by using CG model, we speed up our calculation by sacrificing some details. Therefore, we have to make sure it does not affect the main features of studied system.

Free energy calculation is another big branch under development. For a given system at finite temperature, the minimum free energy gives the ground state of the system and represents equilibrium structure of the system. But in a limited-time MD simulation, the system is easily trapped in a local minimum instead of a global one, which cannot reflect the correct structure of the system and all the possible transient states in reaction (e.g., protein folding). Free energy calculation has been developed to solve this problem. Accelerated MD running, umbrella sampling and metadynamics are all used to explore phase space, and have achieved certain success.

Finally, we mention that coupling all the simulations at different levels and integrating them into a unique program is a time-consuming and hard-working task. That is why the Nobel prize in chemistry in 2013 was awarded to Martin Karplus, Michael Levitt and Arieh Warshel "for the development of multiscale models for complex chemical systems." More about multiscale modeling and simulation can be found in reference [59].

1.4 References

[1] K. S. Novoselov, A. K. Geim, S. Morozov, D. Jiang, Y. Zhang, S. Dubonos, I. Grigorieva and A. Firsov, Science **306**, 666-669 (2004).

[2] K. S. Novoselov, D. Jiang, F. Schedin, T. J. Booth, V. V. Khotkevich, S. V. Morozov and A. K. Geim, Proc. Natl. Acad. Sci. U.S.A. **102**, 10451-10453 (2005).

[3] A. C. Neto, F. Guinea, N. Peres, K. S. Novoselov and A. K. Geim, Rev. Mod. Phys. **81**, 109 (2009).

[4] A. K. Geim and K. S. Novoselov, Nature Mater. **6**, 183-191 (2007).

[5] P. R. Wallace, Phys. Rev. **71**, 622 (1947)

[6] J. McClure, Phys. Rev. **108**, 612 (1957).

[7] D. DiVincenzo and E. Mele, Phys. Rev. B **29**, 1685 (1984).

[8] S. Morozov, K. Novoselov, M. Katsnelson, F. Schedin, D. Elias, J. Jaszczak and A. Geim, Phys. Rev. Lett. **100**, 016602 (2008).

[9] K. I. Bolotin, K. Sikes, Z. Jiang, M. Klima, G. Fudenberg, J. Hone, P. Kim and H. Stormer, Solid State Commun. **146**, 351-355 (2008).

[10] K. Novoselov, A. K. Geim, S. Morozov, D. Jiang, M. K. I. Grigorieva, S. Dubonos and A. Firsov, Nature **438**, 197-200 (2005).

[11] V. Gusynin and S. Sharapov, Phys. Rev. Lett. **95**, 146801 (2005).

[12] Y. Zhang, Y.-W. Tan, H. L. Stormer and P. Kim, Nature **438**, 201-204 (2005).

[13] C. Lee, X. Wei, J. W. Kysar and J. Hone, Science **321**, 385-388 (2008).

[14] R. Nair, P. Blake, A. Grigorenko, K. Novoselov, T. Booth, T. Stauber, N. Peres and A. Geim, Science **320**, 1308-1308 (2008).

[15] H. Wang, D. Nezich, J. Kong and T. Palacios, IEEE Electron Device Lett. **30**, 547-549 (2009).

[16] F. Xia, T. Mueller, Y.-m. Lin, A. Valdes-Garcia and P. Avouris, Nat. Nanotechnol. **4**, 839-843 (2009).

[17] R. Nair, H. Wu, P. Jayaram, I. Grigorieva and A. Geim, Science **335**, 442-444 (2012).

[18] X. Wang, L. Zhi and K. Mllen, Nano Letters **8**, 323-327 (2008).

[19] Q. Yan, B. Huang, J. Yu, F. Zheng, J. Zang, J. Wu, B.-L. Gu, F. Liu and W. Duan, Nano Letters **7**, 1469-1473 (2007).

[20] F. Schwierz, Nat. Nanotechnol. **5**, 487-496 (2010).

[21] S. Amini, J. Garay, G. Liu, A. A. Balandin and R. Abbaschian, J. Appl. Phys. **108**, 094321 (2010).

[22] Y. Zhang, C. Hui, R. Sun, K. Li, K. He, X. Ma and F. Liu, Nanotechnology **25**, 135301 (2014).

[23] A. K. Geim, Science **324**, 1530-1534 (2009).

[24] M. S. Fuhrer, C. N. Lau and A. H. MacDonald, MRS Bull. **35**, 289-295 (2010).

[25] D. R. Dreyer, R. S. Ruoff and C. W. Bielawski, Angew. Chem. Int. Ed. **49**, 9336-9344 (2010).

[26] A. Neto and K. Novoselov, Rep. Prog. Phys. **74**, 82501-82509 (2011).

[27] S. Stankovich, D. A. Dikin, R. D. Piner, K. A. Kohlhaas, A. Kleinhammes, Y. Jia, Y. Wu, S. T. Nguyen and R. S. Ruoff, Carbon **45**, 1558-1565 (2007).

[28] D. Chen, H. Feng and J. Li, Chem. Rev. **112**, 6027-6053 (2012).

[29] Y. Hernandez, V. Nicolosi, M. Lotya, F. M. Blighe, Z. Sun, S. De, I. McGovern, B. Holland, M. Byrne and Y. K. Gun'Ko, Nat. Nanotechnol. **3**, 563-568 (2008).

[30] A. B. Bourlinos, V. Georgakilas, R. Zboril, T. A. Steriotis and A. K. Stubos, Small **5** (16), 1841-1845 (2009).

[31] R. J. Smith, M. Lotya and J. N. Coleman, New J. Phys. **12**, 125008 (2010).

[32] X. Wang, P. F. Fulvio, G. A. Baker, G. M. Veith, R. R. Unocic, S. M. Mahurin, M. Chi and S. Dai, Chem. Commun.
46, 4487-4489 (2010).

[33] K. R. Paton, E. Varrla, C. Backes, R. J. Smith, U. Khan, A. ONeill, C. Boland, M. Lotya, O. M. Istrate, P. King, T. Higgins, S. Barwich, P. May, P. Puczkarski, I. Ahmed, M. Moebius, H. Pettersson, E. Long, J. Coelho, S. E. OBrien, E. K. McGuire, B. M. Sanchez, G. S. Duesberg, N. McEvoy, T. J. Pennycook, C. Downing, A. Crossley, V. Nicolosi and J. N. Coleman, Nat Mater. **13**, 624-630 (2014).

[34] J. N. Coleman, M. Lotya, A. ONeill, S. D. Bergin, P. J. King, U. Khan, K. Young, A. Gaucher, S. De and R. J. Smith, Science **331**, 568-571 (2011).

[35] V. Nicolosi, M. Chhowalla, M. G. Kanatzidis, M. S. Strano and J. N. Coleman, Science **340** 1226419 (2013).

[36] S. Malik, A. Vijayaraghavan, R. Erni, K. Ariga, I. Khalakhan and J. P. Hill, Nanoscale **2**, 2139-2143 (2010).

[37] X. Li, W. Cai, J. An, S. Kim, J. Nah, D. Yang, R. Piner, A. Velamakanni, I. Jung and E. Tutuc, Science **324**, 1312-1314 (2009).

[38] T. Ohta, A. Bostwick, T. Seyller, K. Horn and E. Rotenberg, Science **313**, 951-954 (2006).

[39] C. Virojanadara, M. Syvjarvi, R. Yakimova, L. Johansson, A. Zakharov and T. Balasubramanian, Phys. Rev. B **78**, 245403 (2008).

[40] T. Welton, Chem. Rev. **99**, 2071-2084 (1999).

[41] P. Wasserscheid and W. Keim, Angew. Chem. Int. Ed. **39**, 3772-3789 (2000).

[42] R. D. Rogers and K. R. Seddon, Science **302**, 792-793 (2003).

[43] S. Zhang, N. Sun, X. He, X. Lu and X. Zhang, J. Phys. Chem. Ref. Data **35**, 1475-1517 (2006).

[44] J. P. Hallett and T. Welton, Chem. Rev. **111**, 3508-3576 (2011).

[45] M. Koel, Ionic liquids in chemical analysis. (CRC Press, 2008).

[46] N. D. Khupse and A. Kumar, Indian J. Chem., Sect. A, **49**, 635 (2010).

[47] H. Niedermeyer, J. P. Hallett, I. J. Villar-Garcia, P. A. Hunt and T. Welton, Chem. Soc. Rev. **41**, 7780-7802 (2012).

[48] N. V. Plechkova and K. R. Seddon, Chem. Soc. Rev. **37**, 123-150 (2008).

[49] R. Petrenko and J. Meller, eLS (2010). DOI: 10.1002/9780470015902.a0003048.pub2

[50] M. P. Allen, in Computational soft matter: from synthetic polymers to proteins, edited by N. Attig, R. Binder, H. Grubmuller, K. Kremer. (Julich: John von Neumann Institute for Computing, 2004), Vol. 23, pp.1-28.

[51] F. Ercolessi, A molecular dynamics primer. spring college in computational physics. (ICTP, Trieste, 1997).

[52] M. P. Allen and D. J. Tildesley, Computer simulation of liquids. (Oxford University Press, 1987).

[53] A. R. Leach, Molecular modelling: principles and applications. (Pearson Education, 2001).

[54] D. Frenkel and B. Smit, Understanding molecular simulation: from algorithms to applications. (Academic Press, 2001).

[55] D. C. Rapaport, The art of molecular dynamics simulation. (Cambridge University Press, 2004).

[56] J. Tersoff, Phys. Rev. B **37**, 6991 (1988).

[57] D. W. Brenner, Phys. Rev. B **42**, 9458 (1990).

[58] D. W. Brenner, O. A. Shenderova, J. A. Harrison, S. J. Stuart, B. Ni and S. B. Sinnott, J. Phys.: Condens. Matter **14**, 783 (2002).

[59] Coarse-graining of condensed phase and biomolecular systems, edited by Gregory A. Voth (CRC Press, 2008)

CHAPTER 2

MOLECULAR DYNAMICS SIMULATION OF GRAPHENE EXFOLIATION PROCESS USING IONIC SURFACTANT

This chapter discusses in detail the study of the dynamic process in liquid system, specifically, the MD simulation of the SDS surfactant/water + bilayer graphene mixture system. Two mechanisms of graphene exfoliation are investigated: changing the interlayer distance and sliding away the relative distance. By calculating the total energy as a function of the interlayer (sliding-away) distance at different surface-coverage concentrations of SDS surfactant (SDS concentrations), we obtain the separation energy barriers underlying the two mechanisms and their dependence on SDS concentration. Overall, in the first process, the energy barrier can only be reduced by the SDS slightly, and the remaining energy barrier is still too high for graphene exfoliation to be viable. In the second process, the energy barrier can first be decreased continuously with the increasing SDS concentration until it almost completely disappears in the optimal SDS concentration range (1.5-2.0/nm^2). The barrier then increases again with the further increase of SDS concentration. Therefore, the sliding-away mechanism is identified as the more viable separation process. The analysis of SDS anion density profile on the graphene surface indicates that the graphene-surfactant interaction plays an important role in the separation process by stabilizing the separated graphene sheet.

2.1 Introduction

Graphene is a two-dimensional, one atom thick honeycomb lattice made of *sp*-bonded carbon atoms [1,2], which is also the basic building block of graphite, carbon nanotubes, fullerenes and so on. Because of its extraordinary electronic, mechanical and optical properties, it has attracted a wide range of research attention [3-6]. Although fundamental research is still carried out on graphene [7,8], more and more attention is being paid to its potential applications such as transistors [9], electrodes [10], solar cells [11], supercapacitors

[12] and biodevices [13]. To realize its potential applications, however, mass production of high quality graphene must be achieved.

The high quality yet small-piece graphene produced by using the micromechanically cleavage method has been used in fundamental investigation of its properties, but it is not suitable for large-scale, easy and cheap mass production [14]. The development of large-scale, high-quality graphene growth method has drawn a lot of attention and progressed rapidly in the past decade. Segregation of carbon from carbon-saturated metals (Ni/Fe) [15], chemical vapor deposition on metal substrates [16], epitaxial growth on silicon carbide [17] and graphite oxide reduction [18] have been explored with certain success, but they either suffer from the difficulty of integrating the sample into devices [14] or disrupting the intrinsic electronic structure of graphene [18].

Recently, an alternative top-down liquid exfoliation approach to producing cheap, large-scale graphene has been proposed [19], which has also been extended to separating other layered materials [20,21]. In these solution-phase techniques, raw material such as graphite powder was first prepared and then dispersed in organic solvents or aqueous surfactant solutions. Shock wave was generated by sonication which breaks apart the graphite flakes. After removing the aggregates by centrifugation, a homogeneous liquid dispersion including separated monolayer and few-layer graphene was obtained. The separated graphene has been stabilized by the attachment of solvent molecules on the surface of graphene. A key point of this method is that the surface energy of solvent molecules has to match that of graphite, which can make the separated graphene stable [22].

Based on the experience of dispersions of carbon nanotubes, Coleman's group has shown that N-Methylpyrrolidone (NMP) and N, N-Dimethylacetamide (DMA) are efficient at dispersing graphene [23], and improved their dispersion by using cheap, low-boiling, safe and user-friendly surfactants/water mixture solution [24]. Bourlinos and Stubos have found some perfluorinated aromatic molecules such as hexafluorobenzene (C_6F_6) and octafluorotoluene ($C_6F_5CF_3$) which can also be used to prepare solubilized graphenes [25]. Some other liquid exfoliation studies have also been reported by using a wide range of solvents [26-31].

By using surface energy and Hansen solubility parameter data analysis, Coleman and co-workers have shown that solvent-graphene surface matching is the dominating factor in the dispersion process [22]. This semiempirical approach can provide us with some useful information in discovering new solvents; however, it does not give a complete, clear picture of understanding the dispersion process. On the other hand, molecular dynamics simulations

have been widely used to study the complicated liquid systems for a long time. Important solvents such as water, surfactant, Ionic liquids and their mixture systems with carbon nanotube (or graphite) have been studied. Especially, Blankschtein and co-workers have studied graphene/polar solvents systems and explained the stabilization of the graphene sheets by calculating potential of mean force and kinetic theory analysis [32]. Later, they also studied ionic surfactant sodium cholate (SC) on a monolayer graphene sheet and calculated electrostatic potential around graphene-SC assembly [33]. Most recently, Yang and Fu have studied the interfacial mechanics for different solvents and concluded that the confined solvent molecules between graphene sheets contribute significantly to the exfoliation and stabilization process [34].

However, SDS as an important ionic surfactant, which is composed of positively charged sodium ions and anions with a long nonpolar carbon tail, plays an important role in separating graphite and has not been studied systematically. In order to better understand the liquid dispersion of graphene, SDS/water + graphene mixture system need to be investigated. The separation mechanism, the role of SDS concentration and corresponding surface morphology are all interesting questions remaining to be answered.

In this paper, we have carried out MD simulations of SDS/water + bilayer graphene mixture system at a variety of surface-coverage concentrations of SDS surfactant (SDS concentrations). By calculating the total energy as a function of interlayer (sliding-away) distance, we obtain the energy barrier and surface morphology at different SDS concentrations. Then we studied surfactant distribution along separation path (interlayer or sliding-away distance). We compared these two separation mechanisms and analyzed the role of SDS concentration in each process.

2.2 Simulation Methodology

In this work, the classical all-atom MD simulations were done by GROMACS package [35]. The total potential energy is given by the expression:

$$V = \sum_{bonds} k_b(r - r_{eq}) + \sum_{angles} k_\theta(\theta - \theta_{eq}) + \sum_{dihedrals} \frac{v_n}{2}(1 + cos(n\phi - \gamma)) + \sum_i \sum_{j>i} (\frac{a_{ij}}{r_{ij}^{12}} - \frac{b_{ij}}{r_{ij}^{6}} + \frac{q_{ij}}{r_{ij}}) \quad (2.2.1)$$

In the above equation, the first three terms and latter two terms describe the intramolecular and intermolecular interactions, respectively. The force field parameters for SDS are provided from the standard Amber force field. As for the model of graphene, we choose a rigid-body model which only considers the VdW interaction between different graphene

layers [36] and takes parameters suggested in the literature [37]. This model ignores the intramolecular interactions within graphene, and hence atomic vibration and small bond distortion during graphene exfoliation process. This should be a good approximation because these effects will not significantly influence the separation energy barrier, which is dominated by the intermolecular interactions, i.e., the graphene-graphene and graphene-surfactant interaction. The water model is TIP3P [38] which is compatible with Amber force Field. The partial charges for the anion of SDS were calculated by fitting ab initio electrostatic potentials with RESP package [39] , while the charge of sodium ion and carbon atoms in graphene are +1, 0 , respectively. The ab initio calculation was done with Gaussian 03 package [40].

The system studied in this work consists of SDS surfactant/water + bilayer graphene mixture. The structure of SDS is shown in Fig. 2.1. The ion pairs in surfactant, number of atoms in bilayer graphene and number of water molecules in different SDS concentration are given in Table 2.1. The initial simulation configuration was randomly generated by Gromacs package followed by a quick relaxation, and then the relaxed configuration was simulated with a constant NPT simulation for 8ns at room temperature (T=298.15K) and the total energy of the last 3ns was calculated. To make sure the system reaches the equilibrium, an annealing process was then used; the final configuration obtained from the NPT simulation was again equilibritated at T=1000K in a constant NVT simulation and the temperature was gradually lowered to 800K, 600K, 400K and room temperature. We repeated the annealing process two or three times. Finally, the production run of NVT simulation at room temperature was carried out for 3ns. All the data are taken from this period. The timestep used in the simulations is 1fs, while the cutoff of 12 Å for VdW interaction is used. Long-range electrostatic interactions were treated using the particle mesh Ewald (PME)

Table 2.1. Size of the SDS surfactant/water + bilayer graphene simulation system

SDS concentration ($/nm^2$)	Number of carbon atoms (graphite)	Number of ion pairs (SDS)	Number of water molecules
0	2800	0	9281
0.5	2800	70	9281
1.0	2800	140	9281
1.5	2800	216	9281
2.0	2800	280	9281
2.8	2800	393	9281

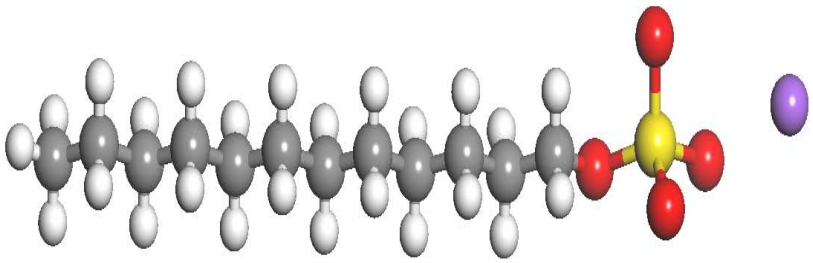

Figure 2.1. The structure of SDS molecule. The gray, white, red, yellow and purple balls represent carbon, hydrogen, oxygen, sulfur and sodium atoms, respectively.

summation method [41,42]. Berendsen coupling is used for maintaining a pressure of 1 atm in NPT simulations and velocity rescales were used in all the simulations [43].

2.3 Results and Discussion

In this section, we talk about our simulation results in two processes of exfoliation mechanism, comparing these two methods.

2.3.1 Graphene Exfoliation by Variation of Interlayer Distance (Fig. 2.2a)

To simulate the exfoliation process, we consider the variation of the interlayer distance of bilayer graphene at six different SDS concentrations by calculating the total energy as a function of interlayer distance (Fig. 2.3). The two large, parallel single-layer graphene sheets have been put in a big box form an AA-stacked bilayer graphene. The interlayer distance r varies from about 3 Å to 12 Å. By extracting the data from the production run, the relative total energy (potential energy) profile is shown in Fig. 2.3 (we take the energy at $r = 3.4$ Å as our reference of zero energy). In addition, the average numbers of SDS anions confined in between the graphene sheets are also calculated and shown in Fig. 2.4.

From Fig. 2.3, we found that the minimum energies in the mixture systems are all located at the distance r around 3.6 Å, which is slightly larger than the equilibrium layer-layer distance of pure graphite (3.35 Å). This can be understood by the attractive interaction between graphene and solvent.

There are three major (solvent-solvent, solvent-graphene and graphene-graphene) interactions in the mixture system compared to one (graphene-graphene) interaction in pure bilayer graphene system, the competition between graphene-graphene and solvent-graphene interaction changes the equilibrium separation distance which varies slightly with SDS concentration as shown in Fig. 2.3. The energy increases quickly for 3.4 Å $< r <$ 6 Å, indicating that the graphene-graphene VdW interaction still dominates in the mixture system. With the increasing distance r, the energy oscillates for 6 Å $< r <$ 12 Å and the systems finally reach the complete separation of the bilayer graphene at $r = 12$ Å. From 6 Å to 12 Å, two more local minima form, which means the solvent-graphene interaction begins to dominate and gradually overcome the graphene-graphene interaction. From Fig. 2.3 and Fig. 2.4(a), we discover a corresponding relationship between the confined number of SDS anions in between two graphene sheets and the potential energy profile. For $r < 7$ Å, because of a too small space, no SDS anions can be confined. Then there is a quick increase of confined number of SDS anions and they form one layer of SDS (7 Å $<= r <=$ 9

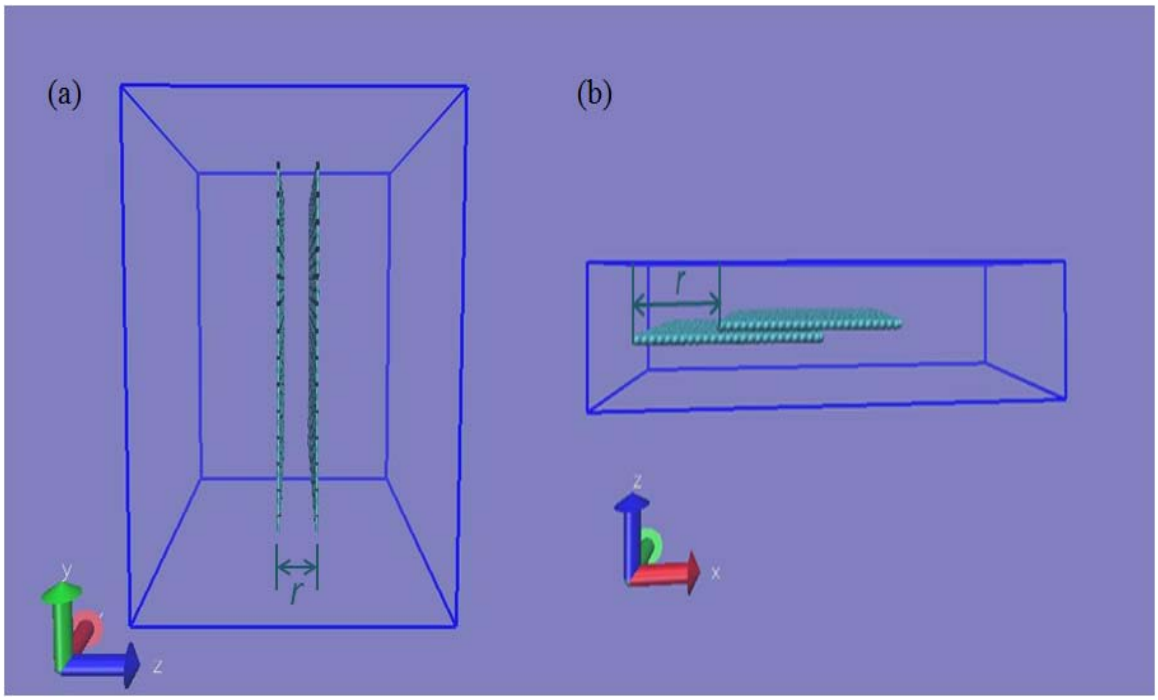

Figure 2.2. Graphene separation mechanism. (a) Schematic graph of variation of interlayer distance of two parallel single-layer graphene sheets; (b) Schematic graph of variation of sliding away distance of two single-layer graphene sheets. Blue is the simulation box and green is graphene.

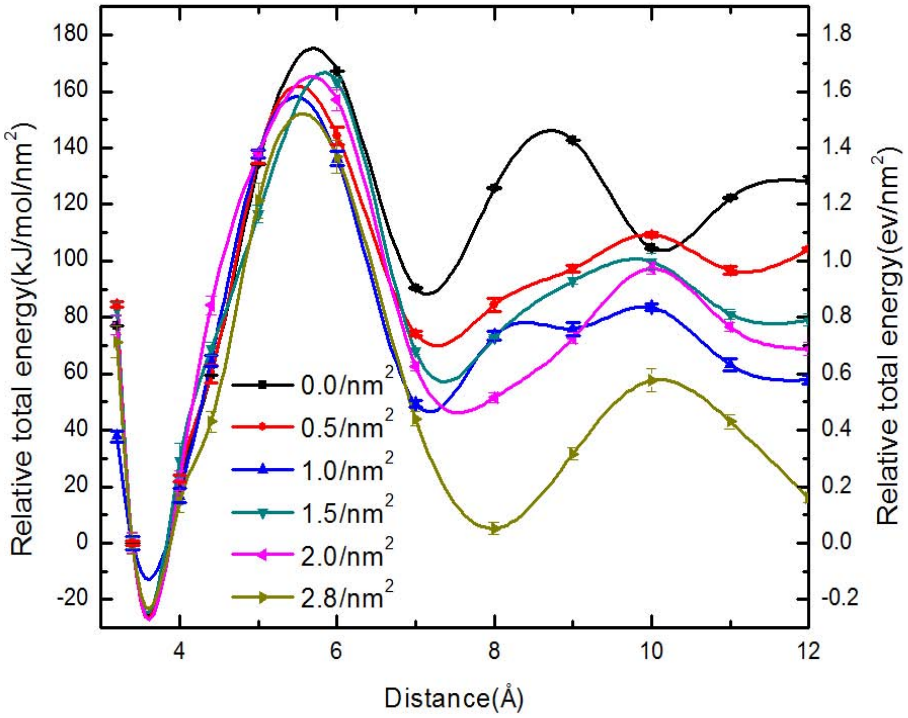

Figure 2.3. Relative total energy (potential energy profile) of SDS surfactant/water + bilayer graphene mixtures at different SDS concentrations as a function of interlayer distance.

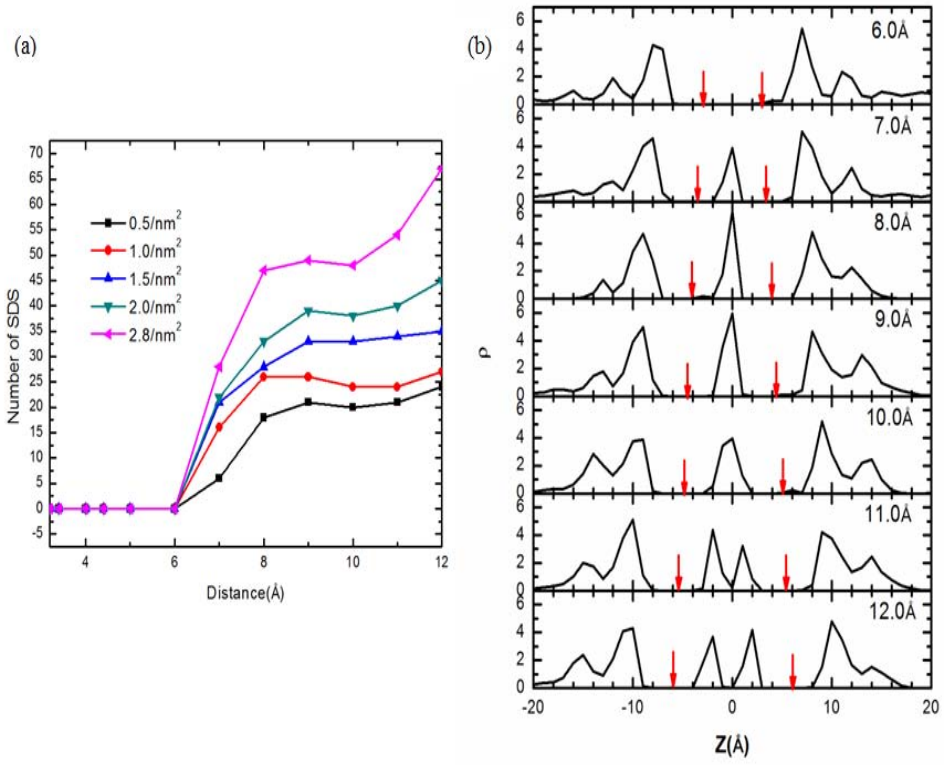

Figure 2.4. SDS anion distribution analysis in SDS surfactant/water + bilayer graphene mixture system. (a) Number of SDS anions confined in inner space between two parallel single-layer graphene sheets. (b) Normalized density profile of SDS anions as a function of interlayer distance at SDS concentration=2.0/nm^2. (The red arrows give the locations of two graphene sheets.)

Å), which contributes to the first local minimum in Fig. 2.3. Then we have a short range for almost no change of the number of confined SDS anions (still one layer SDS) for 9 Å <= r < 11 Å, which contributes to the local maximum at $r \approx 10$ Å. For r >= 11 Å, the number of SDS anions increases again and two layers of SDS form. Here we need to point out the black line in Fig. 2.3, which shows the potential energy profile along the separation distance in water + bilayer graphene system (no SDS). Similar to SDS surfactant/water + bilayer graphene system, the confinement of water molecules in between two graphene sheets contributes to two local minima at $r \approx 7$, 10 Å. This suggests that water has a weak interaction with graphene. However, even at very large separation distances, the energy of water + bilayer graphene system is still high, which means the separated graphene state is not as stable as in SDS surfactant/water solution. Therefore, water alone cannot effectively lower the separation energy barrier of bilayer graphene because of weaker surface affinity of water on graphene surface. The following discussion will be focused on the role of SDS concentrations.

To see the transitions clearly, we plot SDS anion density profile along z axis (interlayer distance) and extract snapshots at different SDS concentrations. Because of the similarity at all concentrations, here we only show the plots at SDS concentration = 2.0/nm^2 (Fig. 2.4b). Since there are no SDS anions confined inside the interlayer graphene inner space at small distances, the plot begins with distance r > 6 Å. When 7 Å <= r <= 10 Å, There is one peak inside the interlayer graphene inner space in Fig. 2.4b. Because the graphene-graphene VdW interaction disappears quickly after moving further away from the graphite equilibrium distance, SDS anions have been attracted into the open space and total energy attains a local minimum here at around 7 $\sim$ 8 Å. In this region, we found the number of SDS anions first increases, then stabilizes (almost no change or slight decrease). This is consistent with Fig. 2.3, because after the local minimum at r around 7 Å, the energy increases and reaches a local maximum at r around 10 Å. Further increasing the distance from the local maximum, the number of SDS anions increases again and forms two layers, and correspondingly the energy decreases again. The zero layer, one layer and two layers of SDS in between the two graphene sheets are also shown in snapshots of Fig. 2.5. The forming of the SDS layers in between the two graphene sheets can be understood as the attractive interaction between SDS anions and graphene drives more and more SDS anions to move into the inner space between two graphene sheets when interlayer distance increases. The number of SDS anions increases gradually to form one layer and two layers of SDS until completely separating the graphene sheets.

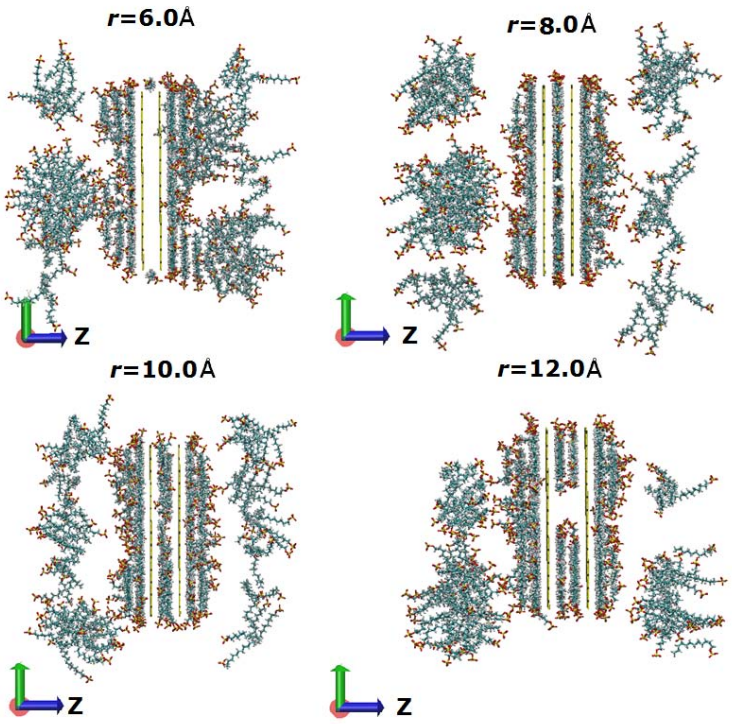

Figure 2.5. Snapshots from production run at 4 different interlayer distances. SDS concentration = 2.0/nm^2. We only show SDS anions and graphene sheet to make it clear. Red represents oxygen in SDS, yellow represents graphene and cyan represents tail of SDS anion.

From the potential energy profile (Fig. 2.3), we can define local energy barriers of the separation process at different SDS concentrations, and the calculated results are shown in Table 2.2. From Table 2.2, we can see that compared with water + bilayer graphene system without SDS which has a first and second barrier (2.0 eV/nm^2 and 0.6 eV/nm^2), both the first and second energy barriers are smaller in the SDS surfactant/water + bilayer graphene mixture system at different SDS concentrations which means the SDS surfactant/water + bilayer graphene system is better than water + bilayer graphene system in separating graphene. However, the decreases of energy barrier by SDS via this direct separation process is insignificant by ∼0.1-0.3 eV. This indicates that direct changing interlayer distance is unlikely the most viable mechanism of separation. Therefore, below we investigate a different mechanism.

2.3.2 Graphene Exfoliation by Sliding Away the Relative Distance of Graphene (Fig. 2.2(b))

In the above considered mechanism of bilayer graphene exfoliation by changing the interlayer distance, strong VdW interaction between graphene sheets must be overcome. Because the separation path is parallel to the VdW interaction direction, it is energy consuming compared to another possible exfoliation path: sliding away the relative distance of graphene. Here again, we calculate the total energy as a function of sliding-away distance at different SDS concentrations; the distance varies from about 3.4 Å to 7.0 nm (complete separation). The calculated results are shown in Fig. 2.6 (the energy at r= 3.4 Å as the reference of zero energy). As we can see, when the SDS concentration is smaller or equal to 1.0/nm^2, the energy generally goes up with the increasing sliding-away distance. The energy oscillates at SDS concentration = 1.5 (or 2.0)/nm^2 when the sliding-away distance increases, with no obvious trend. The energy curve at SDS concentrations of 2.8/nm^2 shows a strong oscillation compared with that at SDS concentrations of 1.5 (or 2.0) /nm^2, and

Table 2.2. Energy barriers in variation of interlayer distance mechanism

SDS concentration (/nm^2)	First energy barrier (eV/nm^2)	Second energy barrier (eV/nm^2)
0	2.0	0.6
0.5	1.9	0.4
1.0	1.7	0.4
1.5	1.9	0.4
2.0	1.9	0.5
2.8	1.7	0.5

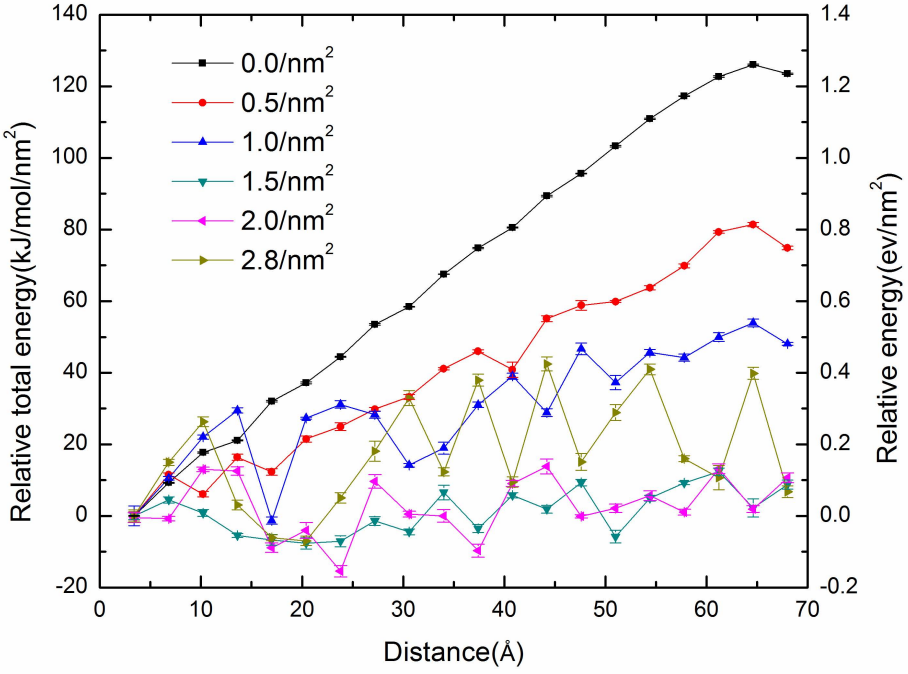

Figure 2.6. Relative total energy (potential energy) profile of SDS surfactant/water + bilayer graphene mixtures at different SDS concentrations as a function of sliding-away distance.

seems to increase slowly with the increasing sliding-away distance, similar to those at SDS concentrations <= 1.0/nm^2. When we use a linear function to fit these energy curves, the slope of each fit can tell us the increasing rate of the energy curve. When slope > 0, the energy still increases as the sliding-away distance increases, and larger slope means a harder separation process. For slope ≈ 0, the energy curve basically does not go up with the increasing sliding-away distance, which means an easier separation process. Our fit slopes for 6 different SDS concentrations are 2.06, 1.24, 0.54, 0.22 -0.02 and 0.31, respectively. Then we calculated the energy barrier in this process (the energy difference between the maximum state and the initial state). From the calculated results shown in Table 2.3, we found that the energy barrier decreases as the SDS concentration increases, from 0.5/nm^2 to SDS concentration of 1.5/nm^2, at which there is a minimum barrier of 0.12 eV/nm^2, and then it increases to 0.4 eV/nm^2 at SDS concentration = 2.8/nm^2 .

Therefore, for the best bilayer graphene separation, SDS concentration is around 1.5-2.0/nm^2. This can be understood as follows: when there is no surfactant, the dominant interaction is graphenen-graphene VdW interaction, which decreases quickly with the increasing sliding-away distance. When adding surfactants into the system, increasing sliding-away distance means more surface area of graphene is exposed to solvents, and more surfactants are attracted to the exposed surface, which lower the energy compared to water + bilayer graphene system. At low SDS concentrations (<= 1.0/nm^2), the graphene-surfactant interaction is not strong enough to compensate the total loss of the graphene-graphene VdW interaction when sliding away graphene sheet, the energy increases. While at higher SDS concentrations (<= 2.0/nm^2), the graphene-surfactant interaction becomes so strong and sufficiently compensates the energy lost of the graphene-graphene VdW interaction, which makes no obvious change of the energy. At maximum SDS concentration (= 2.8/nm^2), the graphene-surfactant interaction becomes weaker again, so the energy goes up again. Other

Table 2.3. Energy barriers in variation of sliding-away distance mechanism

SDS concentration (/nm^2)	energy barrier (eV/nm^2)
0	1.26
0.5	0.81
1.0	0.54
1.5	0.12
2.0	0.13
2.8	0.4

interactions perturb the energy and make the energy curve oscillate. From the analysis above, we conclude that at the critical SDS concentrations (1.5-2.0/nm^2, when slope $\approx$ 0), the energy barrier almost disappears, which is the best for graphene separation.

Apparently, the graphene-surfactant interaction plays an important role in decreasing the separation energy barrier. We plot the SDS anion density profile along the separation path (x axis) and snapshots at SDS concentration = 2.0/nm^2 (Fig. 2.7 and Fig. 2.8). Before the separation, the SDS self-assembles to form big micelles (Fig. 2.8), which lowers the energy and makes the system a stable state. When we increase the sliding-away distance, the attractive graphene-surfactant interaction forces SDS to move to the exposed surface of graphene which compensates the loss of graphene-graphene interaction. So the micelle structure has been destroyed gradually and the entire graphene surface has been covered with SDS. The attachment of SDS on graphene surface gives the maximum graphene-surfactant interaction and stabilizes the separated graphene sheets.

2.4 References

[1] K. S. Novoselov, A. K. Geim, S. Morozov, D. Jiang, Y. Zhang, S. Dubonos, I. Grigorieva and A. Firsovr, Science **306**, 666-669 (2004).

[2] K. S. Novoselov, D. Jiang, F. Schedin, T. J. Booth, V. V. Khotkevich, S. V. Morozov and A. K. Geim, Proc. Natl. Acad. Sci. U.S.A. **102**, 10451-10453 (2005).

[3] A. K. Geim and K. S. Novoselov, Nature Mater. **6**, 183-191 (2007).

[4] C. Lee, X. Wei, J. W. Kysar and J. Hone, Science **321**, 385-388 (2008).

[5] A. K. Geim, Science **324**, 1530-1534 (2009).

[6] K. S. Novoselov, V. Fal, L. Colombo, P. Gellert, M. Schwab and K. Kim, Nature **490**, 192-200 (2012).

[7] A. C. Neto, F. Guinea, N. Peres, K. S. Novoselov and A. K. Geim, Rev. Mod. Phys. **81**, 109 (2009).

[8] S. D. Sarma, S. Adam, E. Hwang and E. Rossi, Rev. Mod. Phys. **83**, 407 (2011).

[9] Q. Yan, B. Huang, J. Yu, F. Zheng, J. Zang, J. Wu, B.-L. Gu, F. Liu and W. Duan, Nano Lett. **7**, 1469-1473 (2007).

[10] K. S. Kim, Y. Zhao, H. Jang, S. Y. Lee, J. M. Kim, K. S. Kim, J.-H. Ahn, P. Kim, J.-Y. Choi and B. H. Hong, Nature **457**, 706-710 (2009).

[11] Y. Zhang, C. Hui, R. Sun, K. Li, K. He, X. Ma and F. Liu, Nanotechnology **25**, 135301 (2014).

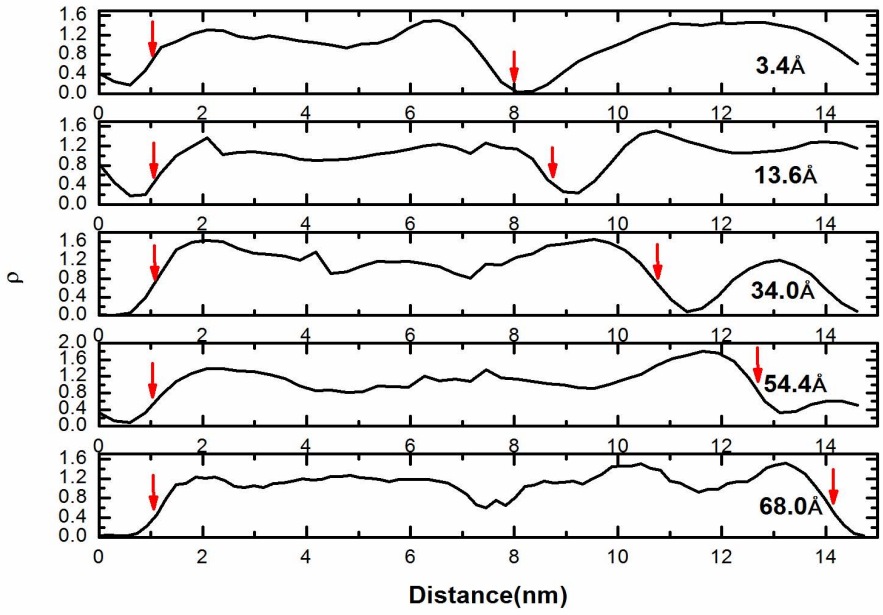

Figure 2.7. Normalized density profile of SDS as a function of sliding-away distance at SDS concentration=2.0/nm^2. (The red arrows give the locations of two graphene sheets edges.)

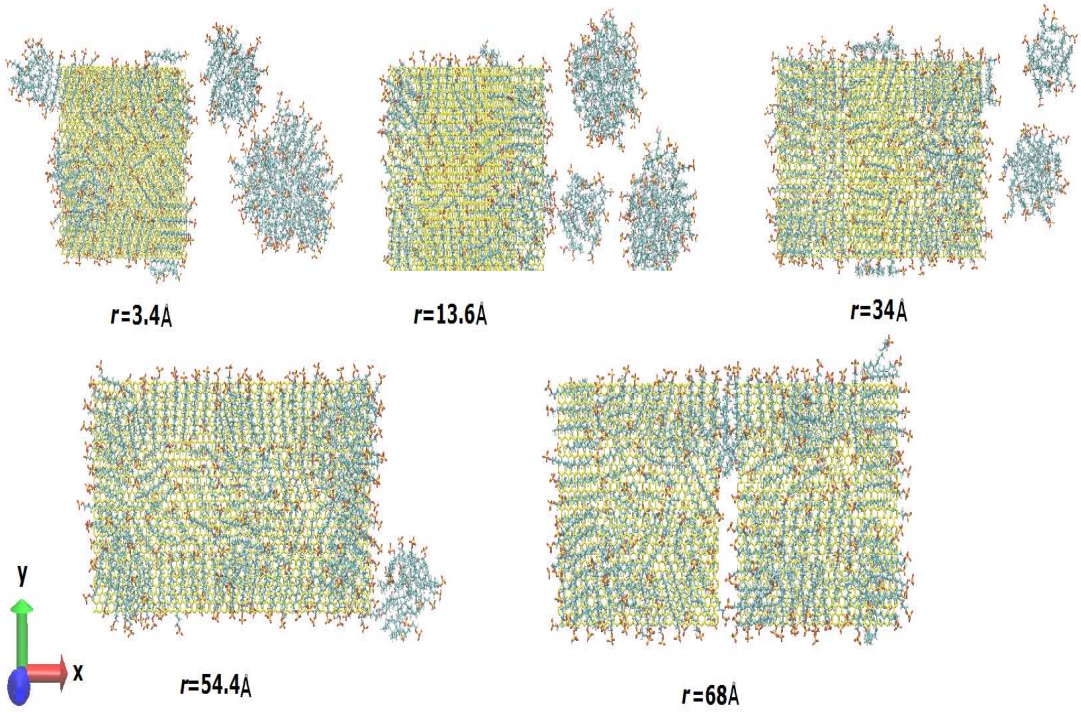

Figure 2.8. Snapshots from production run at 5 different sliding away distances (SDS concentration=2.0/nm^2. Only SDS anions and graphene sheet are shown to make it clear.) Red represents oxygen in SDS, yellow represents graphene and cyan represents the tail of SDS.

[12] Y. Zhu, S. Murali, M. D. Stoller, K. Ganesh, W. Cai, P. J. Ferreira, A. Pirkle, R. M. Wallace, K. A. Cychosz and M. Thommes, Science **332**, 1537-1541 (2011).

[13] R. Nair, P. Blake, J. Blake, R. Zan, S. Anissimova, U. Bangert, A. Golovanov, S. Morozov, A. Geim and K. Novoselov, Appl. Phys. Lett. **97**, 153102 (2010).

[14] P. Avouris and C. Dimitrakopoulos, Mater. Today **15**, 86-97 (2012).

[15] Q. Yu, J. Lian, S. Siriponglert, H. Li, Y. P. Chen and S.-S. Pei, Appl. Phys. Lett. **93**, 113103 (2008).

[16] A. Obraztsov, E. Obraztsova, A. Tyurnina and A. Zolotukhin, Carbon **45**, 2017-2021 (2007).

[17] A. Charrier, A. Coati, T. Argunova, F. Thibaudau, Y. Garreau, R. Pinchaux, I. Forbeaux, J.-M. Debever, M. Sauvage-Simkin and J.-M. Themlin, J. Appl. Phys. **92**, 2479-2484 (2002).

[18] S. Stankovich, D. A. Dikin, R. D. Piner, K. A. Kohlhaas, A. Kleinhammes, Y. Jia, Y. Wu, S. T. Nguyen and R. S. Ruoff, Carbon **45**, 1558-1565 (2007).

[19] A. A. Green and M. C. Hersam, J. Phys. Chem. Lett. **1**, 544-549 (2009).

[20] J. N. Coleman, M. Lotya, A. ONeill, S. D. Bergin, P. J. King, U. Khan, K. Young, A. Gaucher, S. De and R. J. Smith, Science **331**, 568-571 (2011).

[21] V. Nicolosi, M. Chhowalla, M. G. Kanatzidis, M. S. Strano and J. N. Coleman, Science **340** 1226419 (2013).

[22] J. N. Coleman, Acc. Chem. Res. **46**, 14-22 (2012).

[23] Y. Hernandez, V. Nicolosi, M. Lotya, F. M. Blighe, Z. Sun, S. De, I. McGovern, B. Holland, M. Byrne and Y. K. Gun'Ko, Nat. Nanotechnol. **3**, 563-568 (2008).

[24] M. Lotya, Y. Hernandez, P. J. King, R. J. Smith, V. Nicolosi, L. S. Karlsson, F. M. Blighe, S. De, Z. Wang and I. McGovern, J. Am. Chem. Soc. **131**, 3611-3620 (2009).

[25] A. B. Bourlinos, V. Georgakilas, R. Zboril, T. A. Steriotis and A. K. Stubos, Small **5**, 1841-1845 (2009).

[26] J. Lu, J.-x. Yang, J. Wang, A. Lim, S. Wang and K. P. Loh, ACS Nano **3**, 2367-2375 (2009).

[27] X. Wang, P. F. Fulvio, G. A. Baker, G. M. Veith, R. R. Unocic, S. M. Mahurin, M. Chi and S. Dai, Chem. Commun. **46**, 4487-4489 (2010).

[28] R. J. Smith, M. Lotya and J. N. Coleman, New J. Phys. **12**, 125008 (2010).

[29] B. J. van Wees, Chem. Commun. **46**, 7539-7541 (2010).

[30] S. BittoloBon, J. Mater. Chem. **21**, 3428-3431 (2011).

[31] J. Zhao, Z. Wang, Q. Zhao and B. Xing, Environ. Sci. Technol. **48**,331-339, (2014).

[32] C.-J. Shih, S. Lin, M. S. Strano and D. Blankschtein, J. Am. Chem. Soc. **132**, 14638-14648 (2010).

[33] S. Lin, C.-J. Shih, M. S. Strano and D. Blankschtein, J. Am. Chem. Soc. **133**, 12810-12823 (2011).

[34] C. Fu and X. Yang, Carbon **55**, 350-360 (2013).

[35] E. Apol, R. Apostolov, H. Berendsen, A. Van Buuren, P. Bjelkmar, R. Van Drunen, A. Feenstra, G. Groenhof, P. Kasson and P. Larsson, Gromacs user manual 4.5.4. (Royal Institute of Technology and Uppsala University: Stockholm and Uppsala, Sweden 2010).

[36] D. Yu and F. Liu, Nano Lett. **7**, 3046-3050 (2007).

[37] L. Battezzati, C. Pisani and F. Ricca, J. Chem. Soc., Faraday Trans. 2 **71**, 1629-1639 (1975).

[38] W. L. Jorgensen, J. Chandrasekhar, J. D. Madura, R. W. Impey and M. L. Klein, J. Chem. Phys **79**, 926-935 (1983).

[39] C. I. Bayly, P. Cieplak, W. Cornell and P. A. Kollman, J. Phys. Chem. **97**, 10269-10280 (1993).

[40] M. J. Frisch, G. W. Trucks, H. B. Schlegel et al., GAUSSIAN 03, Revision C.02, Gaussian, Inc., Wallingford, CT, 2004.

[41] T. Darden, D. York and L. Pedersen, J. Chem. Phys **98**, 10089-10092 (1993).

[42] U. Essmann, L. Perera, M. L. Berkowitz, T. Darden, H. Lee and L. G. Pedersen, J. Chem. Phys **103**, 8577-8593 (1995).

[43] H. J. Berendsen, J. P. M. Postma, W. F. van Gunsteren, A. DiNola and J. Haak, J. Chem. Phys **81**, 3684-3690 (1984).

CHAPTER 3

NANOSTRUCTURAL ORGANIZATION IN ACETONITRILE/IONIC LIQUID MIXTURES: MD SIMULATIONS

In Chapter 2, we have presented the MD simulation of the dynamic process of graphene liquid exfoliation, The following two chapters (3 and 4) cover the MD simulation study of mesoscopic structures and intermolecular interactions in small solute molecules/IL mixture systems. Small solute molecules that mimic the functional groups in macromolecules are used to explore the role of ILs in the mixture system, which is important for application of ILs. We discuss two kinds of solutes: polar and nonpolar ones. In this chapter, the nanostructural organization in mixtures of acetonitrile (polar solute) and the ionic liquid 1-pentyl-3-methylimidazolium bis{(trifluoromethane) sulfonyl} amide ($[C_5mim][NTf_2]$) are studied as a function of concentration using MD simulations. The MD simulations show that IL nanostructurally organizes into an ionic network and nonpolar domains with CH_3CN molecules localized in the interfacial region between the ionic network and nonpolar domains, in agreement with previous findings by other researchers. The MD simulations also indicate strong interactions between CH_3CN and the hydrogens on the imidazolium ring of the cation, which competes with the CH_3CN-cation interaction that induces the disruption of ionic networks. The nonpolar solute/IL mixture will be discussed in Chapter 4.

3.1 Introduction

Room temperature ionic liquids are a class of compounds that have been extensively investigated as environmentally benign solvents in synthesis, electrochemistry, separations, and other applications [1,2]. Their potential as green "designer" solvents stems from their negligible vapor pressure, ease of recycling, and the ability to vary their properties by changing the structure of the ions [3-5]. In order to optimize the use of ILs for various applications, their physicochemical properties must be understood at a molecular level.

Wang and Voth [6], using a multiscale coarse-graining MD approach, found that ILs based on the l-alkyl-3-methylimidazolium ion ($[C_n mim]^+$) are nanosegregated into polar domains with the cation rings and anions homogeneously distributed and nonpolar domains formed by the aggregation of alkyl groups for C_4 and longer. This result was subsequently more completely analyzed [7] and also confirmed by all-atom MD simulations [8,9]. Using the all-atom MD method, it was further shown [8] that the polar domains are not isolated but are interconnected in such a way as to form a three-dimensional charge-ordered ionic network permeated by nonpolar domains in a manner resembling that of a swollen gel.

Indirect evidence for this structural heterogeneity has been found in Raman (linear and nonlinear) spectroscopic measurements [10,11]. However, the experimental observation commonly presented as evidence for this structural heterogeneity is the appearance of a first sharp diffraction peak or prepeak at $Q_{MAX} < 0.5$ Å^{-1} in the small-wide angle X-ray scattering (SWAXS) data corresponding to a correlation length D $= 2\pi/Q_{MAX}$ that varies linearly with alkyl chain length. This prepeak has been observed in imidazolium salts with $[BF4]^-$, $[PF6]^-$, $[Cl]^-$ [12-14], and bis{(trifluoromethane)sulfony}amide ($[NTf_2]^-$]) [15-17], in alkylammonium nitrates with alkyl = ethyl and propyl [18], in phosphonium-based salts [19], aliphatic quaternary salts [20], and in protic ionic liquids [21].

To obtain a microscopic understanding of this prepeak, Hardacre et al. [14] performed small angle neutron scattering (SANS) measurements on H/D isotopically, substituted $[C_n mim][PF6]$ with $n = 4$, 6, and 8. Difference scattering spectra showed that spatial correlations of the imidazolium headgroup, and to a lesser extent, C_n groups, contribute to the prepeak. In addition, the peak position in real space calculated from the inverse of the peak position in Q-space of these ILs and maximum second-shell cation-cation separation in the radial distribution function (RDF) for $[C_1 mim][PF_6]$ derived from SANS data exhibit a linear dependence on the length of the cation. This relationship between the peak position and the length of the cation led Hardacre et al. to propose that the peak is a "result of expansion in the second shell cation-cation coordination lattice, most probably due to the interspacing of alkyl-chain substituents." They found that spatially resolved probability distributions of anions and cations around a central imidazolium derived from empirical potential structure refinement (EPSR) models are similar for the three ILs with the alkyl chains causing asymmetry in the distributions.

Using an approach that combined computer simulations with X-ray scattering data Annapureddy et al.[22] further clarified the geometrical origin of the prepeak. The basis for their approach was the observation that for imidazolium-based ILs, the peaks below 2 Å^{-1}

in the structure function $S(Q)$ of the liquid are often found in the powder spectrum of the crystal. By tracking the simulated $S(Q)$ through the melting transition, Annapureddy et al. showed that these peaks shifted to lower Q-values with the peak at 0.9 Å^{-1} becoming a shoulder on the peak at 1.5 Å^{-1} in the liquid phase. Simulations of $[C_6mim][Cl]$ and $[C_8mim][PF_6]$ indicate that the way in which polar groups avoid nonpolar groups is the same for the liquid and the crystal. Annapureddy et al. showed, by resolving $S(Q)$ into subcomponents, that for ILs with short chains that the prepeak is attributed to the anion and the nitrogen atoms on the imidazolium ring and not the carbon atoms. This result indicates that the prepeak is associated with an inverse length scale between charged groups. They confirmed that this feature is associated with charged groups separated by the long cationic alkyl tails by comparing the prepeaks in the structure functions of the liquid and the solid. Moreover, Annapureddy et al. found the intensity of the prepeak could be enhanced by artificially bringing the nearest neighbor polar groups closer together.

As a follow-up to the above studies, Santos et al. [23,34] recently combined SWAXS with MD simulations, to examine the structure of the IL methyltributylammonium bis(trifluoro methane)sulfonylamide ($[N_{1444}][NTf_2]$) over a wide temperature range, spanning the normal liquid and the glassy state. By resolving $S(Q)$ into subcomponents, Santos et al. also came to the same conclusion as did Hardacre et al. and Annapureddy et al. that the prepeak in the SWAXS data for $[N_{1444}][NTf_2]$ is a consequence of solvation shell asymmetry. Despite their conclusions, Hardacre et al., Annapureddy et al., and Santos et al. neither refuted nor confirmed the existence of complex morphologies. Hardacre et al. stated that "a loosely organized sponge-like microphase defined by ribbons or strings of alternating anions and cations cannot be ruled out." Annapureddy et al. further suggested that the micelle-like and the solvation shell asymmetry interpretations could be just different descriptions of the same liquid morphology in ILs. Santos et al. also posited that their interpretation of the prepeak does not preclude the existence of "highly ordered structures spanning long distances and many ions" in some ionic liquids.

MD simulations [8,25,26] indicate that solute-solvent interactions in ILs can be quite complex because of nanosegration. At low concentrations, solute molecules are found in the domains for which the affinity is the greatest. Nonpolar molecules, such as n-hexane, are localized in the nonpolar domains and are excluded from the ionic networks because of the cohesive energy of the charged groups [8], whereas associating solutes, such as water, are mainly localized in the ionic networks, forming strong hydrogen bonds with the charged parts of the ions [8,25,26]. On the other hand, dipolar molecules, such as CH_3CN, interact

with the nonpolar domains as well as with the charged head groups in the ionic networks [8,25]. At high concentrations, the solute molecules eventually disrupt the nanostructural organization and, in the case of water, cause micelles to be formed [26].

In this chapter, we report a study of the nanostructural organization of mixtures of CH_3CN and $[C_5mim][NTf_2]$ using all-atom MD simulations. The corresponding experiment study of subpicosecond intermolecular dynamics of the mixtures have been done by our collaborators Xiao et al. using optical heterodyne-detected Raman-induced Kerr effect spectroscopy (OHD-RIKES). (See Appendix A for more details about experiment.) Although CH_3CN/IL systems have been previously studied using terahertz (THz) spectroscopy [27] to clarify their nature as mixtures of two liquids or electrolyte solutions and by time-resolved Stokes shift techniques to understand their solvation dynamics [28], our collaborated work, to our knowledge, is the first molecular-level study of CH_3CN/IL mixtures combining MD simulations with OHD-RIKES.

The current work is one of a series of papers on the nanostructural organization and intermolecular dynamics of molecular-solvent/IL mixtures. We previously presented results from a study of mixtures of CS_2 and $[C_5mim][NTf_2]$ as a function of the mole fraction of CS_2 [29]. We found that the CS_2 contribution to the optical Kerr effect (OKE) spectrum of a 5 mol % CS_2/$[C_5mim][NTf_2]$ mixture is similar to that of a 5 mol % CS_2/n-pentane mixture [30]. This result is consistent with MD simulations that showed the CS_2 molecules to be separated from each other and located in the interior of the nonpolar domains [29]. We also provided further analysis of the OKE spectra of 15-25 mol % mixtures as well as MD simulations of the 20 mol % mixture that showed nanostructural organization at higher solute concentrations to be quite different than at lower concentrations due to aggregation of the CS_2 molecules.

In this chapter, we discuss how MD simulations provide support for the localization of CH_3CN molecules in the interfacial region between the ionic network and nonpolar domains and the role of CH_3CN in determining the nanostructural organization of CH_3CN/IL mixtures. This chapter is organized as follows. In Section 3.2, we outline the procedures used to perform the MD simulations. In Section 3.3, we present the results of the simulations.

3.2 Models and Simulation Methodology

3.2.1 Atomistic Force Field

The total potential energy is described by the Amber force field given by the expression:

$$V = \sum_{bonds} k_b(r - r_{eq}) + \sum_{angles} k_\theta(\theta - \theta_{eq}) + \sum_{dihedrals} \frac{v_n}{2}(1 + cos(n\phi - \gamma)) + \sum_i \sum_{j>i} (\frac{a_{ij}}{r_{ij}^{12}} - \frac{b_{ij}}{r_{ij}^6} + \frac{q_{ij}}{r_{ij}}) \quad (3.2.1)$$

In the above equation, the force field parameters for $[C_5mim]^+$ are obtained from the standard Amber force field, while the parameters and partial charges for $[NTf_2]^-$ come from the work of Lopes and Padua [31], which is compatible with the Amber force field. The partial charges of the cation were calculated by fitting the ab initio electrostatic potentials with the RESP fitting package [32]. The ab initio calculations were performed with Gaussian 03 [33]. The force field and partial charges for CH_3CN used in our simulations were based on the six-site flexible model developed by Nikitin and Lyubartsev [34].

3.2.2 Molecular Dynamics Simulation Details

In the simulations, the concentrations of the mixtures investigated were 0, 5, 10, 20, and 50 mol %. The number of ion pairs and CH_3CN molecules depends on the computational feasibility. The simulation parameters are given in Table 3.1.

The initial configuration of the mixture system was manually constructed, with the ions and CH_3CN molecules positioned within a large cubic simulation box. The initial configuration was simulated at 300 K at constant NPT for 1-2 ns to get a constant volume. The final configuration was then equilibrated at 1000 K under constant NVT conditions and gradually cooled down to 400 K at temperature intervals of 200 K. At each temperature (1000, 800, 600, 400 K), the system was equilibrated for 1.5 ns. The final configuration was

Table 3.1. Sizes for different simulated $CH_3CN/[C_5mim][NTf_2]$ mixtures.

Mole Percent CH_3CN	Number of ion pairs	Number of solute molecules	Simulation cell size(X,Y,Z),Å
0	64	0	31.4,31.4,31.4
5	76	4	33.4,33.4,33.4
10	72	8	32.8,32.8,32.8
20	64	16	31.8,31.8,31.8
50	64	64	33.1,33.1,33.1

then run at 298 K under constant NVT conditions for 8 ns. All simulations were carried out using the DL_POLY 2.19 package [35] with periodic boundary conditions.

3.2.3 Major Groups and Definitions (Figure 3.1)

The atoms in the system can be divided into three groups: polar, nonpolar, and solute. The polar groups are the positively charged imidazolium ring and the $[NTf_2]^-$ anion, whereas the nonpolar group is the entire alkyl chain. The term cation headgroup (or headgroup) specifically refers to the center of mass of the imidazolum ring. The tail group (or tail) refers to the terminal methyl group on the alkyl chain, which can be approximately described by the carbon atom CT in the tail group. The term NP refers to the nitrogen atom in the $[NTf_2]^-$ anion, which is used to represent approximately the center of mass of the anion. The terms H5 and H4 refer to the hydrogen atoms on the imidazolium ring of the cation. The term YN refers to the nitrogen atom in the CH_3CN molecule. (Definitions of the groups are given in Figure 3.1).

3.3 Nanostructural Organization of CH_3CN/IL Mixtures

In our previous study [29] of CS_2/$[C_5mim][NTf_2]$ mixtures, we showed that because solute-tail interactions are stronger than solute-headgroup or solute-anion interactions, CS_2 molecules are mainly located in the nonpolar domains. In contrast, the probability of finding dipolar solute molecules at or near ionic networks should be higher than in the interior of the nonpolar domains. Figure 3.2 shows the radial distributions functions (RDFs) between the nitrogen atom in CH_3CN and the center of mass of the imidazolium ring of the cation (YN-headgroup), between the nitrogen atom in CH_3CN and the terminal group of the C5-chain (YN-CT), and between the nitrogen atom in CH_3CN and the nitrogen atom on $[NTf_2]^-$ (YN-NP) for 5, 10, 20, and 50 mol % CH_3CN/$[C_5mim][NTf_2]$ mixtures. For 5 mol % CH_3CN/$[C_5mim][NTf_2]$, intensities of the first peak in the YN-CT, YN-headgroup, and YN-NP RDFs are 2.09, 2.02, and 1.71, respectively. In contrast, for 5 mol % CS_2/$[C_5mim][NTf_2]$, intensities of the first peak in the CM-CT, CM-headgroup, and CM-NT RDFs are, respectively, 2.25, 1.48, and 1.66, where the term CM corresponds to the carbon atom in CS_2. For both CS_2 and CH_3CN at a concentration of 5 mol %, solute-tail interactions are stronger than solute-headgroup and solute anion interactions. However, based on the relative intensities of the first peak in these RDFs, CH_3CN-headgroup and CH_3CN-anion interactions are stronger than CS_2-headgroup and CS_2-anion interactions, whereas CH_3CN-tail interactions are weaker than CS_2-tail interactions. These results are

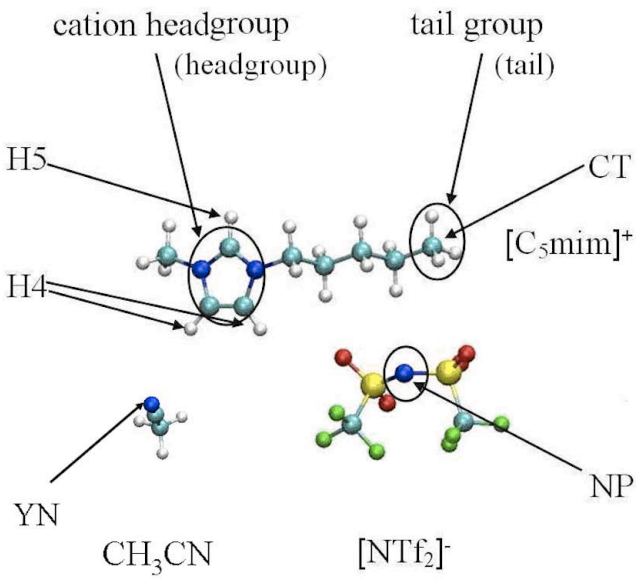

Figure 3.1. The structures of $[C_5mim]^+$, $[NTf_2]^-$, and CH_3CN. The blue balls represent nitrogen atoms, the cyan balls represent carbon atoms, and the white balls represent hydrogen atoms. The red balls represent oxygen atoms, and the green balls represent fluorine atoms. Atom-type definitions: YN is the nitrogen atom in CH_3CN; NP is the nitrogen atom in the anion; CT is the terminal the group on the alkyl chain; and H5, H4 are the hydrogen atoms connected to the cation ring.

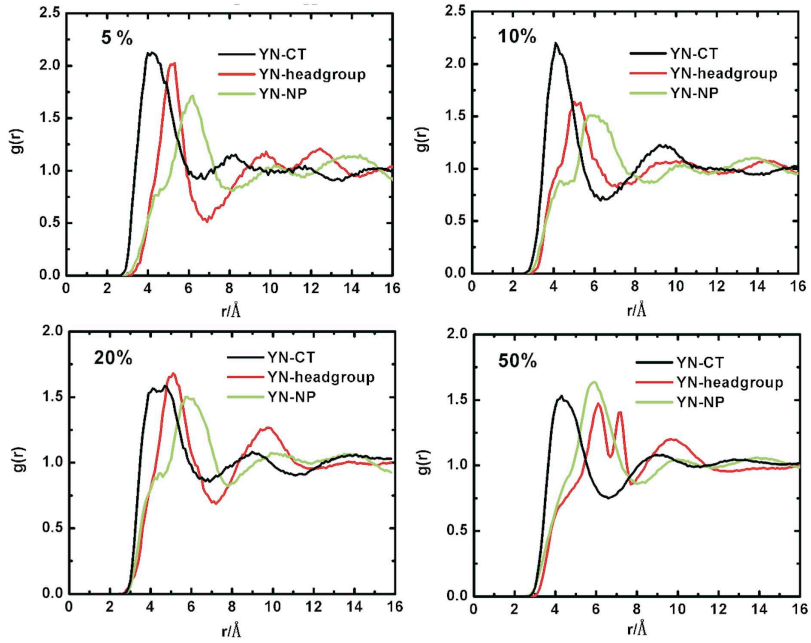

Figure 3.2. Radial distribution functions for the three important interactions in 5, 10, 20, and 50 mol % $CH_3CN/[C_5mim][NTf_2]$. YN-headgroup – nitrogen atom in CH_3CN and the cation headgroup; YN-CT – nitrogen atom in CH_3CN and the CH_3 terminal group on the C_5-chain; YN-NP – nitrogen atom in CH_3CN and the nitrogen atom on $[NTf_2]^-$.

consistent with previous MD simulations of Lopes and coworkers.25,66 When the CH_3CN concentration is increased from 5 to 10 mol %, the intensity of the first peak in the YN-CT RDF increases from 2.09 to 2.16, whereas in the YN-headgroup and YN-NP RDFs, it decreases from 2.02 to 1.64 and from 1.71 to 1.52, respectively. We attribute this behavior in the RDFs to a weakening of the interaction of CH_3CN with the ionic networks and the strengthening of its interactions with the nonpolar domains.

The YN-CT, YN-headgroup, and YN-NP RDFs for 20 and 50 mol % CH_3CN/[C_5mim][N Tf_2] mixtures do not show any evidence for aggregation of CH_3CN at higher concentrations, which is consistent with the observed complete miscibility of CH_3CN with imidazolium-based ILs [36]. Also the intensities of the first peaks in the three RDFs are very similar. Based on these RDFs, we conclude that the negatively charged nitrogen atom of CH_3CN tends to interact with the positively charged headgroup of the cation and the methyl group on CH_3CN with the nonpolar tail group. These two interactions compete with each other to produce the complicated pattern of peaks in the RDFs at the higher solute concentrations. For example, in the RDF of the 50 mol % mixture, the two close peaks at 6.1 and 7.2 in the YN-headgroup RDF suggest that that there two distinct ways in which a CH_3CN molecule can interact with the headgroup of the cation.

In Figure 3.3 are plotted the RDFs between the alkyl tails in the CH_3CN/[C_5mim][NTf_2] mixtures. These RDFs show no obvious trend with concentration, implying that tail-tail interactions are not directly affected by the presence of CH_3CN in the mixture. In contrast, the MD simulations show strong hydrogen bonding between CH_3CN and the headgroup of the cation, as reflected by the intensity of the first peak in the YN-H4 and YN-H5 RDFs of the CH_3CN/[C_5mim][NTf_2] mixtures as depicted in Figure 3.4.

A representative snapshot of the MD trajectory data obtained during a production run for 50 mol % CH_3CN/[C_5mim][NTf_2] is shown in Figure 3.5 with the polar domains colored red, the nonpolar domains colored yellow, and the CH_3CN molecules represented by space-filling structures. Snapshots for the other CH_3CN/[C_5mim][NTf_2] mixtures are similar. Snapshots of the MD trajectory data obtained during production runs for 5, 10, and 20 mol % CS_2/[C_5mim][NTf_2] mixtures revealed structures with solute molecules located inside the nonpolar domain (see Figure 3, ref 54). However, as can be seen in Figure 3.5, such structures are not observed for CH_3CN/[C_5mim][NTf_2] mixtures, which we rationalize as being a consequence of the greater affinity of the dipolar solute CH_3CN for the charged groups than for the alkyl chains. Interestingly, in the snapshots, CH_3CN molecules appear to bridge the nonpolar and the polar domains, with nitrogen atom of the nitrile group pointing

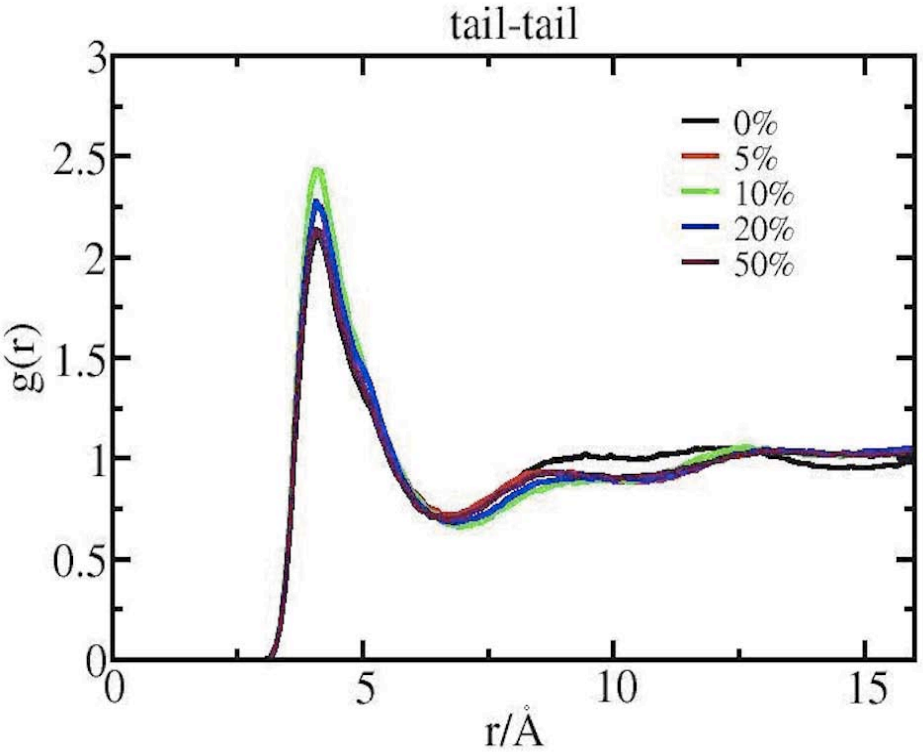

Figure 3.3. Radial distribution function between the alkyl tails in $CH_3CN/[C_5mim][NTf_2]$ mixtures.

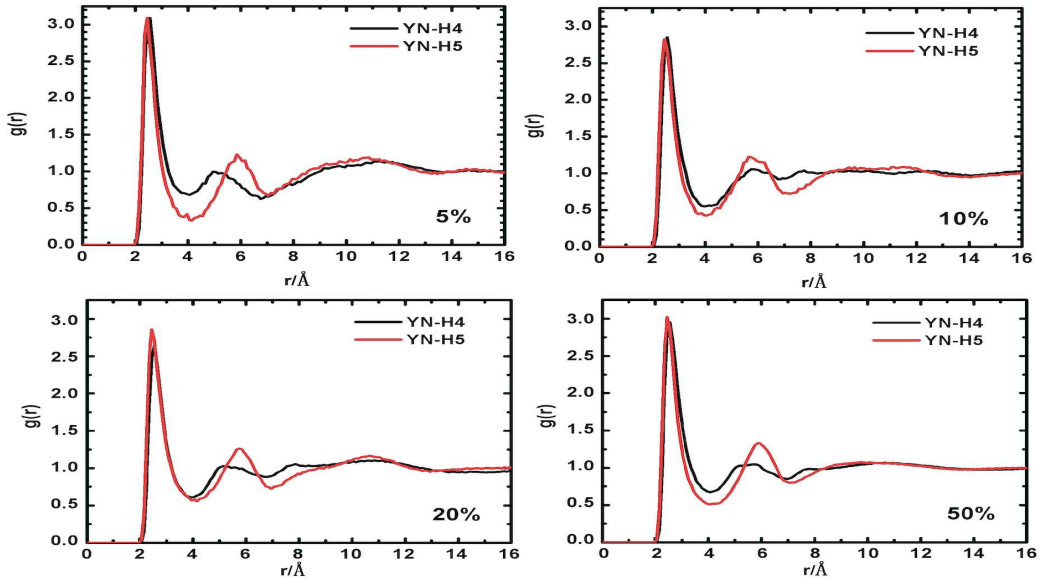

Figure 3.4. Radial distribution function between CH_3CN and the hydrogens and on the imidazolium ring for 5, 10, 15, and 20 mol % $CH_3CN/[C_5mim][NTf_2]$. YN-H4 nitrogen atom in CH_3CN and the H4 hydrogens on the imidazolium ring. YN-H5 nitrogen atom in CH_3CN and the H5 hydrogen on the imidazolium ring.

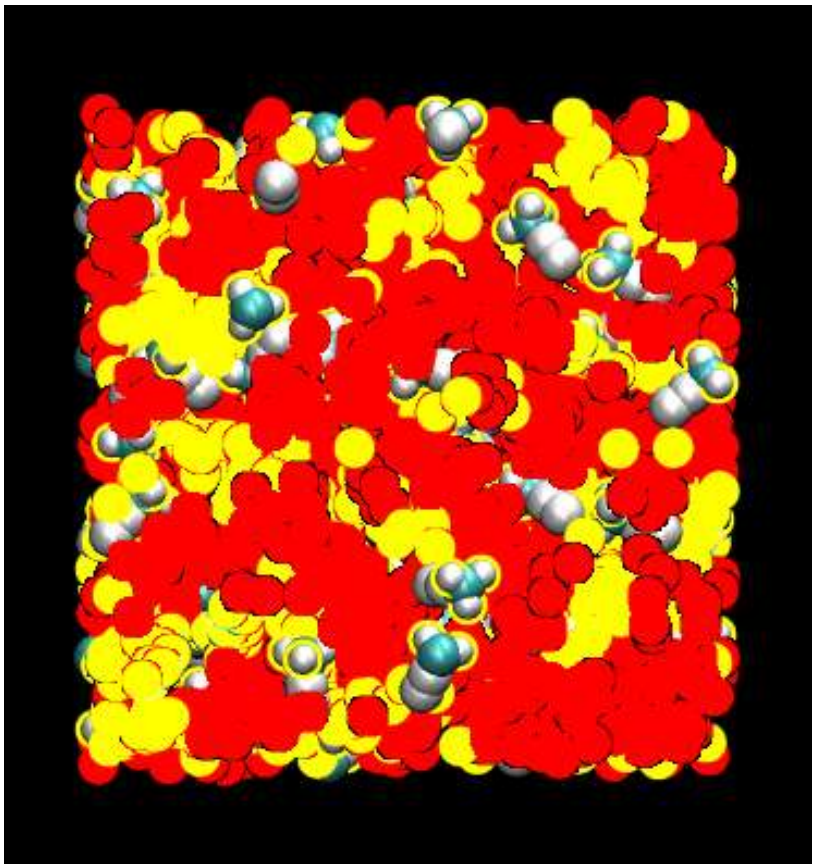

Figure 3.5. Snapshot of the nanostructural organization in 50 mol % CH_3CN/IL mixture, with the polar domains color-coded red, the nonpolar domains color-coded yellow, and the CH_3CN molecules represented by space-filling structures.

toward the positively charged headgroup of the cation and the methyl group residing in the nonpolar domain, which is similar to what was observed previously by Lopes and coworkers [8,25].

Figure 3.6 shows coordination numbers obtained by integrating the RDFs decrease with increasing concentration of CH_3CN. We attribute the decrease in coordination numbers to the weakening of cation-anion interactions with increasing concentration of CH_3CN. The coordination number of CH_3CN-tail group interaction decreases faster than that of CS_2-tail group interaction. This result reflects the competition between CH_3CN-tail group interactions and CH_3CN-headgroup interactions.

3.4 References

[1] Ionic liquids in synthesis, edited by P. Wasserscheid and T. Welton (Wiley VCH, Weinheim, 2007).

[2] N. V. Plechkova and K. R. Seddon, Chem. Soc. Rev. **37**, 123-150 (2008).

[3] M. J. Earle, J. M. S. S. Esperanca, M. A. Gilea, J. N. A. C. Lopes, L. P. N. Rebelo, J. W. Magee, K. R. Seddon and J. A. Widegren, Nature **439**, 831-834 (2006).

[4] M. Freemantle, Chem. Eng. News **76** (13), 32-37 (1998).

[5] N. V. Plechkova and K. R. Seddon, in Methods and reagents for green chemistry: an introduction, edited by P. Tundo, A. Perosa and F. Zecchini (Wiley, New York, 2007), pp. 105-130.

[6] Y. Wang and G. A. Voth, J. Am. Chem. Soc. **127**, 12192-12193 (2005).

[7] Y. Wang and G. A. Voth, J. Phys. Chem. B **110**, 18601-18608 (2006).

[8] J. N. A. C. Lopes and A. A. H. Padua, J. Phys. Chem. B **110**, 3330-3335 (2006).

[9] Y. Wang, W. Jiang and G. A. Voth, in Ionic liquids IV. not just solvents anymore, edited by J. F. Brennecke, R. D. Rogers and K. R. Seddon (American Chemical Society, Washington, DC, 2007), Vol. **975**, pp. 272-307.

[10] S. Shigeto and H. Hamaguchi, Chem. Phys. Lett. **427**, 329-332 (2006).

[11] K. Iwata, H. Okajima, S. Saha and H. Hamaguchi, Acc. Chem. Res. **40**, 1174-1181 (2007).

[12] A. Triolo, O. Russina, H. Bleif and E. Di Cola, J. Phys. Chem. B **111**, 4641-4644 (2007).

[13] A. Triolo, O. Russina, B. Fazio, R. Triolo and E. Di Cola, Chem. Phys. Lett. **457**, 362-365 (2008).

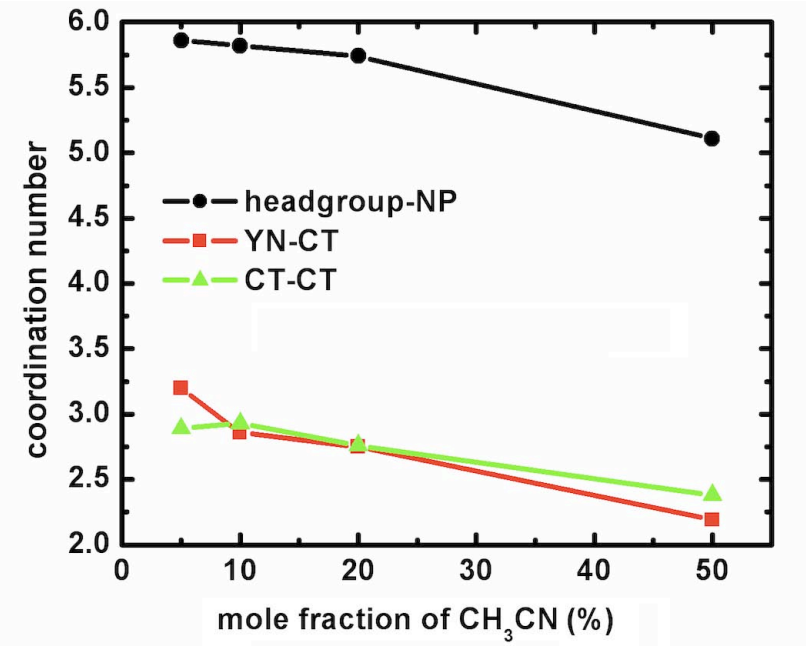

Figure 3.6. Coordination numbers obtained by integration of the radial distributions: headgroup-NP cation headgroup and nitrogen atom on $[NTf_2]_-$; YN-CT – nitrogen atom in CH_3CN and the CH_3 terminal group on the C_5-chain; CT-CT tail-tail.

[13] A. Triolo, O. Russina, B. Fazio, R. Triolo and E. Di cola, Chem. Phys. Lett **457**, 362-365 (2008)

[14] C. Hardacre, J. D. Holbrey, C. L. Mullan, T. G. A. Youngs and D. T. Bowron, J. Chem. Phys. **133**, 074510(074511)-074510(074517) (2010).

[15] D. Xiao, L. G. Hines, Jr., S. Li, R. A. Bartsch, E. L. Quitevis, O. Russina and A. Triolo, J. Phys. Chem. B **113**, 6426-6433 (2009).

[16] O. Russina, M. Beiner, C. Pappas, M. Russina, V. Arrighi, T. Unruh, C. L. Mullan, C. Hardacre and A. Triolo, J. Phys. Chem. B **113**, 8469-8474 (2009).

[17] O. Russina and A. Triolo, Faraday Discuss. **154** (97-109) (2012).

[18] R. Atkin and G. G. Warr, J. Phys. Chem. B **112**, 4164-4166 (2008).

[19] L. Gontrani, O. Russina, F. L. Celso, R. Caminiti, G. Annat and A. Triolo, J. Phys. Chem. B **113**, 9235-9240 (2009).

[20] M. Mizuhata, M. Maekawa and S. Deki, ECS Transactions 3, **89** (2007).

[21] T. L. Greaves, D. F. Kennedy, S. F. Mudie and C. J. Drummond, J. Phys. Chem. B **114**, 10022-10031 (2010).

[22] H. V. R. Annapureddy, H. K. Kashyap, P. M. De Biase and C. J. Margulis, J. Phys. Chem. B **114**, 16838-16846 (2010).

[23] C. S. Santos, H. V. R. Annapureddy, N. S. Murthy, H. K. Kashyap, E. W. Castner Jr and C. J. Margulis, J. Chem. Phys. **134**, 064501(064501)-064501(064510) (2011).

[24] H. K. Kashyap, C. S. Santos, H. V. R. Annapureddy, D. S. N. Murthy, C. J. Margulis and E. W. Castner Jr, Faraday Discuss. **154**, 133-143 (2012).

[25] A. A. H. Padua, M. F. C. Gomes and J. N. A. C. Lopes, Acc. Chem. Res. **40**, 1087-1096 (2007).

[26] W. Jiang, Y. Wang and G. A. Voth, J. Phys. Chem. B **111**, 4812-4818 (2007).

[27] M. L. Asaki, A. Redondo, T. A. Zawodzinski and A. J. Taylor, J. Chem. Phys. **116**, 10377-10385 (2002).

[28] D. Chakrabarty, A. Chakrabarty, D. Seth and M. Sarkar, J. Phys. Chem. A **109**, 1764-1769 (2005).

[29] P. Yang, G. A. Voth, D. Xiao, L. Hines, R. A. Bartsch and E. L. Quitevis, J. Chem. Phys. **135**, 034502(034501)-034502(034512) (2011).

[30] D. Xiao, L. G. Hines, Jr., R. A. Bartsch and E. L. Quitevis, J. Phys. Chem. B **113**, 4544-4548 (2009).

[31] J. N. C. Lopes and A. A. H. Padua, J. Phys. Chem. B **108**, 16893-16898 (2004).

[32] C. I. Bayly, P. Cieplak, W. Cornell and P. A. Kollman, J. Phys. Chem. **97**, 10269-10280 (1993).

[33] M. J. Frisch, G. W. Trucks, H. B. Schlegel et al., GAUSSIAN 03, Revision C.02, Gaussian, Inc., Wallingford, CT, 2004.

[34] A. M. Nikitin and A. P. Lyubartsev, J. Comp. Chem. **28**, 2020-2026 (2007).

[35] W. Smith and T. R. Forester, The DL_POLY_2 user manual. (Daresbury Laboratory, Daresbury, England, 1999).

[36] J. J. Wang, Y. Tian, Y. Zhao and K. Zhuo, Green Chem. **89**, 618-622 (2003).

CHAPTER 4

NANOSTRUCTURAL ORGANIZATION IN CARBON DISULFIDE/IONIC LIQUID MIXTURES: MD SIMULATIONS

This Chapter is a continuation of the discussion of small solute molecule/IL mixture systems from Chapter 3. Here, the nanostructural organization in mixtures of CS_2 (nonpolar solute) and ionic liquid 1-pentyl-3-methyl-imidazolium bis{(trifluoromethane)sulfonyl}amide ($[C_5mim][NTf_2]$) are studied as a function of concentration using MD simulations. At low CS_2 concentrations (< 10 mol % CS_2/IL), the MD simulations indicate that the CS_2 molecules are localized in the nonpolar domains. In contrast, at higher concentrations (≥ 10 mol % CS_2/IL), the MD simulations show an aggregation of the CS_2 molecules. These simulation results are consistent with the subpicosecond intermolecular dynamics study from the OHD-RIKES experiment. The OKE of the mixtures are interpreted in terms of an additivity model with the components arising from the subpicosecond dynamics of CS_2 and the IL. Comparison of the CS_2-component with the OKE spectra of CS_2 in alkane solvents is consistent with CS_2 mainly being localized in the nonpolar domains, even at high CS_2 concentrations, and the local CS_2 concentration being higher than the bulk CS_2 concentration.

4.1 Introduction

RTILs are commonly defined as organic salts with melting points at or below 373 K [1]. An IL is typically composed of a bulky organic cation and an inorganic or organic anion. Because of their novel properties, such as negligible vapor pressure [2], low flammability, and wide liquid range, ILs have been used extensively in electrochemical, analytical, synthetic, and engineering applications [3,4]. The ability to tune the physicochemical properties of ILs by changing the structure of the ions has led to their being called designer solvents [5,6]. Despite the success of this application-driven research, a fundamental understanding of ILs is still rudimentary [7-9]. With the number of simple ILs estimated to be a million and

ternary systems over a trillion [10], a molecular-level understanding of ILs is necessary for the rational design of task-specific ILs.

One of the unique properties of ILs is the nanoscale heterogeneity in their liquid state. A detailed picture of this heterogeneity was first revealed in molecular dynamics simulations of ILs based on the 1-alkyl-3-methylimidazolium cation ($[C_n mim]^+$) [11-16]. Urahata and Ribeiro [11] observed in united-atom MD simulations a low-Q (momentum transfer) peak in the partial structure factor, which they attributed to the occurrence of intermediate range order for C_4 and C_8, but not for shorter chains. Wang and Voth [12], employing a multiscale coarse-graining MD method, discovered that ILs are nanosegregated into polar regions with the cation rings and anions homogeneously distributed and nonpolar regions formed by the aggregation of alkyl groups for C_4 and longer. This result was subsequently more completely analyzed [13] and also confirmed by all-atom MD simulations [14,17]. Using the all-atom MD approach, it was further shown [14] that the polar regions are not isolated but are interconnected in such a way as to form a three-dimensional charge-ordered ionic network permeated by nonpolar regions in a manner not unlike that of a swollen gel.

Signatures of this structural heterogeneity have been found in Raman (linear and nonlinear) spectroscopic measurements [18,19]. However, the experimental observation commonly invoked as being evidence for the existence of structural heterogeneity is the appearance of a first sharp diffraction peak or prepeak at $Q_{MAX} < 0.5$ Å^{-1} in the small-wide angle X-ray scattering data corresponding to a correlation length D $= 2\pi/Q_{MAX}$ that scales linearly with alkyl chain length. This prepeak has been observed in imidazolium salts with $[BF_4]^-$, $[PF_6]^-$, $[Cl]^-$ [20-22], and bis(trifluoromethane)sulfonyamide ($[NTf_2]^-$) [23,24], in alkylammonium nitrates with alkyl = ethyl and propyl [25], in phosphonium-based salts [26], aliphatic quaternary salts [27], and in protic ionic liquids [28].

To understand the microscopic origin of this prepeak, Hardacre et al. [22]. performed small angle neutron scattering measurements on H/D isotopically substituted $[C_n mim][PF_6]$ with $n = 4$, 6, and 8. Difference scattering spectra showed substantial contributions to the prepeak from spatial correlations of the imidazolium headgroup and a much smaller contribution to the prepeak from spatial correlations of the C_n groups. Moreover, they found that the peak position in real space calculated from the inverse of the peak position in Q-space of these ILs together with the maximum second-shell cation-cation separation in the radial distribution function for $[C_1 mim][PF_6]$ derived from SANS data exhibit a linear dependence on the length of the cation. Based on this relationship between the peak position and the length of the cation, Hardacre et al. concluded that the peak is a result of expansion

in the second shell cation-cation coordination lattice, most probably due to the interspacing of alkyl-chain substituents. To elucidate the liquid structure, Hardacre et al. created models using the empirical potential structure refinement approach. Spatially resolved probability distributions of anions and cations around a central imidazolium derived from EPSR models are similar for the three ILs with the alkyl chains causing asymmetry in the distributions.

Annapureddy et al. [29]. combined detailed computer simulations with experimental data to further clarify the geometrical origin of the prepeak. Their approach was based on the observation that for imidazolium-based ILs, the peaks below 2 Å^{-1} in the structure function S(Q) of the liquid are often present in the powder spectrum of the crystal. For example, in the powder spectrum of $[C_{10}mim][PF_6]$, the peak below 0.5 Å^{-1} arises from reflections from [1,0,0] Miller planes, which coincide with the loci of polar groups of neighboring ions separated by the long alkyl groups. The peak at 0.9 Å^{-1} is assigned to [1,1,-1] and [3,0,0] Miller planes, which coincide with the loci of polar groups of adjacent ions not separated by long alkyl groups, whereas the intense peak at 1.5 Å^{-1} arises from scattering from a large number of different crystal planes, with those that are intermolecular in nature being associated with short close contact distances between ions. By following the simulated $S(Q)$ through the melting transition, Annapureddy et al. showed that these features shifted to lower Q-values with the peak at 0.9 Å^{-1} becoming a shoulder on the peak at 1.5 Å^{-1} in the liquid phase. Simulations of $[C_6mim][Cl]$ and $[C_8mim][PF_6]$ indicate that the structure of the liquid is such that the polar groups avoid the nonpolar groups in a manner similar to that of the crystal. By resolving $S(Q)$ into subcomponents, Annapureddy et al. showed that for these shorter chain ILs the nitrogen atoms and the anion and not the carbon atoms are responsible for the prepeak, thus indicating that its origin is associated with an inverse length scale between polar groups. A comparison of the prepeaks in the structure functions of the liquid and the solid suggests that the spectral feature is associated with charged groups separated by the long cationic alkyl tails. Annapureddy et al. confirmed the interpretation of the prepeak by showing that its intensity can be enhanced by artificially bringing the nearest neighbor polar groups closer together.

Although Hardacre et al. and Annapureddy et al. are in agreement that the prepeak arises from the anisotropy of the cation that results in a directional polarization of the orientation of the cations around the anions, they differ in their conclusions regarding the correlation of the C_n groups. Based on the observation that alkyl-alkyl correlations show a much smaller contribution to the prepeak than what would be expected in a clustered, micelle-like nanostructure, Hardacre et al. concluded that the SANS data do not support

the existence of alkyl domains that persist through the structure of the liquid. Annapureddy et al., however, showed by group analysis of the C-C contribution to $S(Q)$ that the small alkyl contribution to the prepeak can be explained by the cancellation of peaks in the headgroup-headgroup and tail-tail subcomponents through the negative interference of a trough in the tail-headgroup component. Indeed, the C-C RDFs calculated from the simulations indicate that the terminal carbon of a C_n group is most likely to be found closest to terminal carbons of other C_n groups. Hardacre et al. suggested that the correlation length between cations being longer than the length of a single C_n group could represent the gap between two cations separated by their corresponding alkyl chains. Hardacre et al. and Annapureddy et al. are in agreement that their results do not refute or confirm the existence of complex morphologies. Hardacre et al. suggested that a loosely organized sponge-like microphase defined by ribbons or strings of alternating anions and cations cannot be ruled out. Moreover, Annapureddy et al. stated that the micelle-like picture and the solvation shell asymmetry interpretation could be just different ways of describing the same liquid morphology in ILs.

Because of nanosegration into nonpolar and polar domains in ILs, solute-solvent interactions in ILs can be quite complex as indicated by MD simulations [14,15,30] of polar, nonpolar, and associating solutes in ILs. At low concentrations, solute molecules are found in the domains for which the affinity is the greatest. Nonpolar molecules, such as n-hexane, tend to reside in the nonpolar domains and are excluded from the ionic networks because of the cohesive energy of the charged groups [14], whereas associating solutes, such as water, reside mainly in the ionic networks, forming strong hydrogen bonds with the charged part of the ions [14,15,30]. On the other hand, dipolar molecules, such as acetonitrile, interact with the nonpolar domains as well as the charged head groups in the ionic networks [14,30]. At high concentrations, the presence of solute molecules eventually leads to disruption of the nanostructural organization and, in the case of water, to the evolution of micellar structures [15].

Xiao et al. [31] studied the optical Kerr effect spectrum of CS_2 in $[C_5mim][NTf_2]$ as a function of concentration at 295 K using optical heterodyne-detected Raman-induced Kerr effect spectroscopy, in which they showed by assuming that the CS_2 and $[C_5mim][NTf_2]$ contributions to the spectrum of 5 mol % CS_2 in $[C_5mim][NTf_2]$ are separable that the CS_2 contribution is similar to the OKE spectrum of 5 mol % CS_2 in n-pentane with the spectrum being lower in frequency and narrower than that of neat CS_2. These results suggested that at this concentration, CS_2 molecules are isolated from each other and mainly localized in the

nonpolar domains of the IL. Recently, Fruchey and Fayer [32] used the rotational diffusion of charged and uncharged fluorescent probes to show that the dynamics are different in the nonpolar domains than in the polar domains. However, to our knowledge this preliminary study by Xiao et al. is the first to provide information about the nature of the intermolecular dynamics in the nonpolar domains.

In the current chapter, we present new results from MD simulations of 5, 10, and 20 mol % CS_2/[C_5mim][NTf_2] mixture systems. This chapter is organized as follows. In Section 4.2, we outline the procedures used to perform the MD simulations. In Section 4.3, we present the results of the MD simulations. The MD simulations provide support for the localization of CS_2 molecules in the nonpolar domains for concentrations less than 10 mol % and the aggregation of CS_2 for concentrations greater than or equal to 10 mol %. The corresponding experiment finds that the mixture OKE spectrum shifts to lower frequency and becomes narrower with increasing mole fraction of CS_2. This dependence on composition can be accounted for by an additivity model that is given by the sum of a CS_2 contribution arising from the intermolecular vibrational motions of CS_2 molecules in the nonpolar domains and an IL contribution arising from the intermolecular vibrational motions in the polar domains. Comparison of the CS_2 contribution to the OKE spectrum of the 25 mol % mixture with the OKE spectrum of CS_2 in alkane solvents suggests that the local concentration of CS_2 is higher than the bulk concentration, which we attribute to the tendency of CS_2 molecules to reside in the nonpolar domains. The measurement, analysis and main result of the corresponding experiment which is done by Xiao et al. can be seen in Appendix A in detail.

4.2 Models and Simulation Methodology

4.2.1 Atomistic Force Field

The total potential energy is described by the Amber force field given by the expression

$$V = \sum_{bonds} k_b(r - r_{eq}) + \sum_{angles} k_\theta(\theta - \theta_{eq}) + \sum_{dihedrals} \frac{v_n}{2}(1 + cos(n\phi - \gamma)) + \sum_i \sum_{j>i} (\frac{a_{ij}}{r_{ij}^{12}} - \frac{b_{ij}}{r_{ij}^6} + \frac{q_{ij}}{r_{ij}}) \quad (1)$$

In the above equation, the force field parameters for $[C_5mim]^+$ are provided from the standard Amber force field, while the parameters and partial charges for $[NTf_2]^-$ come from the work of Lopes and Padua [33] which are compatible with the Amber force field. As for the model of liquid CS_2, we chose a rigid-body model that only considers the van der

Waals and Columbic interaction and takes the parameters from the Amber force field. The partial charges of the cation and CS_2 were calculated by fitting the ab initio electrostatic potentials with the RESP fitting package [34]. The ab initio calculations were performed with Gaussian 03 [35].

4.2.2 Molecular Dynamics Simulation Details

In the simulations, the mixtures investigated had CS_2 mole percents of 0, 5, 10 and 20 %. The numbers of ion pairs and CS_2 molecules in each system, which depended on the system size, are given in Table 4.1. Although the $S(Q)$s of these systems were not calculated in this study, the simulation boxes in this study will display prepeaks based on the criterion that that box length must be larger than $2[2\pi/Q_{prepeak}]$ [29]. For $[C_5mim][NTf_2]$, $Q_{prepeak} = 5.5 \pm 0.5$ nm^{-1} [23], which corresponds to a minimum box length of 23 ± 1 Å. As can be seen in Table 4.1, all the systems satisfy this criterion. Mixtures with mole fractions as high as 50 mol % were also simulated. However, because phase separation of the CS_2/IL mixtures is observed above 30 mol %, the simulation results for the 50 mol % mixture are not reported in this paper. (It must be noted that finite size effects affect MD simulations, so simulating the precise point of phase separation is difficult.)

The initial configuration of the mixture system was manually constructed, with the ions and CS_2 molecules positioned within a large cubic simulation box. The initial configuration was then simulated at T = 300 K with a constant NPT simulation for 1-2 ns to achieve an equilibrated constant volume. The final configuration was then equilibrated at T = 1000 K in a constant NVT ensemble and gradually cooled down to T = 400 K at 200 K intervals. At each temperature (1000, 800, 600, 400 K), the system was equilibrated for 1.5 ns. Then the final configuration was run at T = 298 K under constant NVT conditions for 8 ns. A total simulation time of 15-16 ns assures that the systems are fully equilibrated. All simulations were carried out using the DL_POLY 2.19 package [36] with periodic boundary conditions.

Table 4.1. Sizes for different simulated CS_2/$[C_5mim][NTf_2]$ mixtures.

Mole Percent CS_2	Number of ion pairs	Number of solute molecules	Simulation cell size(X,Y,Z),Å
0	64	0	31.4,31.4,31.4
5	76	4	33.4,33.4,33.4
10	72	8	32.9,32.9,32.9
20	64	16	32.0,32.0,32.0

4.2.3 Major Groups and Definitions

The atoms in the system can be divided into three groups: polar, nonpolar, and solute (see Figure 4.1). The polar groups are the positively charged imidazolium ring and the $[NTf_2]^-$ anion, whereas the nonpolar group is the whole alkyl chain. The term cation headgroup (or headgroup) is specifically used to refer to the center of mass of the imidazolum ring, and the tail group(or tail) is used to refer to the terminal methyl group on the alkyl chain, which can be approximately described by the carbon atom CT in the tail group. The term CM refers to the carbon atom on a CS_2 molecule, which is used to represent the center of mass of the CS_2 molecule. The term NP refers to the nitrogen atom in the $[NTf_2]^-$ anion, which is used to represent approximately the center of mass of the anion. The terms H5 and H4 refer to the hydrogen atoms on the imidazolium ring of the cation (All definitions are given in Figure 4.1).

4.3 Nanostructural Organization of CS2/IL Mixtures

Figure 4.2 shows the MD RDFs between the carbon atoms in CS_2 and the center of mass of the imidazolium rings of the cation (CM-headgroup), between the carbon atoms in CS_2 and the terminal group of the C_5-chains (CM-CT), and between the carbon atoms in CS_2 and the nitrogen atom on the $[NTf_2]^-$ anion (CM-NP) for 5, 10, and 20 mol % $CS_2/[C_5mim][NTf_2]$. The intensities of the first peak in the RDFs indicate that at low concentrations (5 and 10 mol %), CM-CT interactions are strong, whereas CM-headgroup and CM-NP interactions are relatively weak. The position of the first peak in the CM-CT, CM-headgroup, and CM-NP RDFs occurs, respectively, at $\approx 4, 5$, and 6 Å. Figures 4.2a and 4.2b also show that as the CS_2 concentration is increased from 5 to 10 mol %, the intensity of the first peak in the CM-CT RDF remains constant ≈ 2.25, whereas there is a decrease in the intensities of first peak in the CM-headgroup and CM-NP RDFs. This behavior in the RDFs is consistent with nonpolar CS_2 molecules interacting more strongly with the nonpolar IL groups than with the polar IL groups and therefore tending to reside in the nonpolar IL domains. A distance calculation shows that, on average, CS_2 molecules are located ≈ 18 Å from each other in the 5 mol % mixture, which is consistent our estimate of 20 Å based on the density and concentration of the mixture. Moreover the position of the first peak in the CM-headgroup RDF at ≈ 5 Å and the CM-NP RDF at ≈ 6 Å is consistent with the CS_2 molecules mainly being located in the interior of the IL nonpolar domains as argued previous by Xiao et al. [31]. on the basis of the OKE spectrum of 5 mol % $CS_2/[C_5mim][NTf_2]$. Figure 4.2c shows that the height of the main peak of the CM-CT

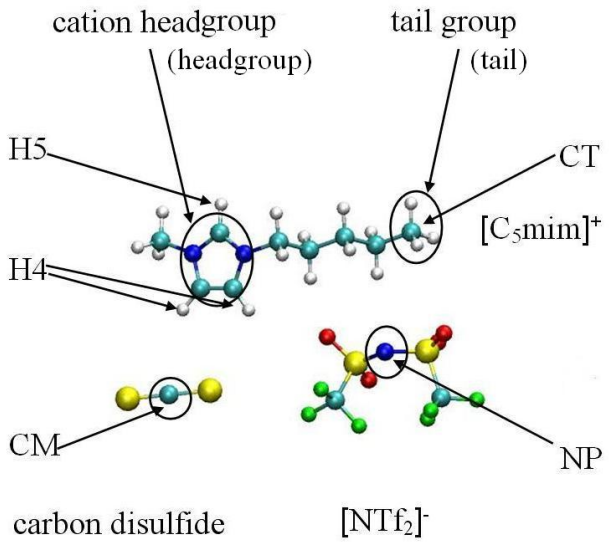

Figure 4.1. The structures of $[C_5mim]^+$, $[NTf_2]^-$, and CS_2 molecules. The blue balls represent nitrogen atoms, the cyan balls represent carbon atoms, and the white balls represent hydrogen atoms. The yellow balls represent sulfur atoms, the red balls represent oxygen atoms, and the green balls represent fluorine atoms. Major group and atom-type definitions are also shown.

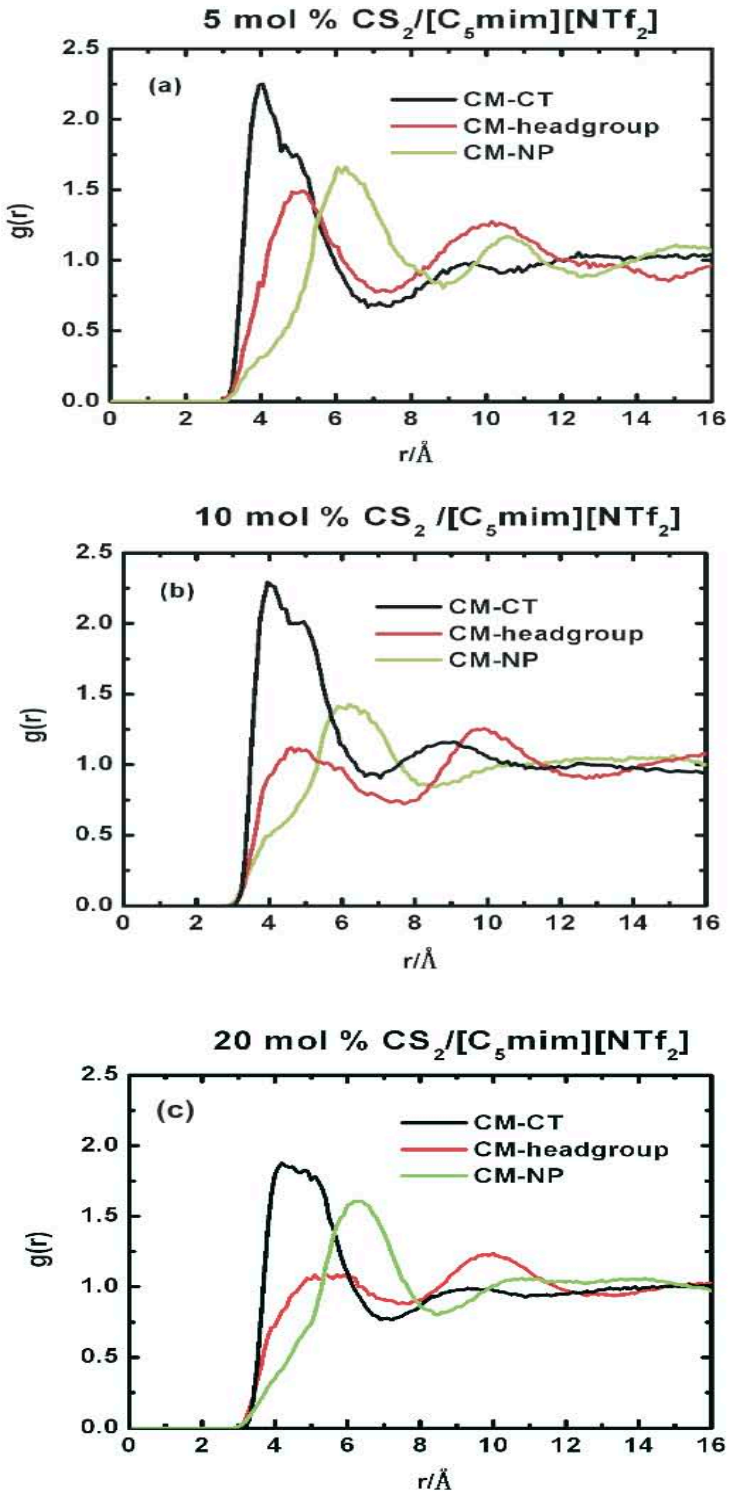

Figure 4.2. Radial distributions functions for three main interactions in (a) 5 mol %; (b) 10 mol %; and 20 mol % CS_2/[C_5mim][NTf_2]. CM-headgroup – carbon atom in CS_2 and the cation headgroup; CM-CT – carbon atom in CS_2 and the CH_3 terminal group on the C_5-chain; CM-NP – carbon atom on CS_2 and the nitrogen atom on $[NTf_2]^-$.

RDF of the 20 mol % mixture is less than 2, which means that CM-CT interactions are weaker at higher concentrations than those at lower concentrations, although this is still the leading interaction in this mixture system. Compared with the CM-CT interaction, the other two interactions (CM-headgroup, CM-NP) interactions are relatively weak.

Figures 4.3a-c depict the nanostructural organization of the 5, 10, and 20 mol % mixtures of CS_2 in $[C_5mim][NTf_2]$. In these figures, the imidazolium rings and anions are not shown for clarity. The figures were taken from snapshots of the MD trajectory data during a production run. These figures clearly show alkyl chain aggregation, which has been shown in previous pure IL MD simulations [12-14]. The new information from these MD simulations is that CS_2 mainly resides in the nonpolar domains because of its strong interactions with the alkyl chains. In the 5 mol % mixture, the CS_2 molecules are isolated from each other, which is consistent with the previous interpretation of the OKE spectrum of 5 mol % $CS_2/[C_5mim][NTf_2]$ by Xiao et al. [31]. However, as the CS_2 mole fraction increases, the local concentration of CS_2 molecules in the nonpolar domains increases. This is evident in the snapshots in Figure 4.3b and 4.3c that show two CS_2 molecules residing in nonpolar domains in the 10 mol % mixture and five CS_2 molecules in nonpolar domains in the 20 mol % mixture.

As mentioned above, at lower concentrations the CS_2 molecules are far away from each other and reside near tails of the C_5-chains. Figure 4.4 depicts the RDF between the carbon atom on a CS_2 molecule and the carbon atom on a different CS_2 (CM-CM interaction) for 5, 10, and 20 mol % $CS_2/[C_5mim][NTf_2]$ mixtures. The height of the first peak in the CM-CM increases with increasing CS_2 mole fraction, suggesting that the composition of the nonpolar domains is becoming richer in CS_2 as depicted in the snapshot in Figure 4.3c.

Figure 4.5 shows RDFs corresponding to cation headgroup-anion and tail-tail interactions in the $CS_2/[C_5mim][NTf_2]$ mixture system. Figure 4.5a shows changes in the intensity of the main peak of the RDF associated with headgroup-NP interactions. However, the position of the main peak in this RDF is unaffected by the addition of CS_2. As for the tail-tail interaction, Figure 4.5b shows no obvious change in the RDF. Interestingly, Cadena et al. [37] found a similar behavior in MD simulations of mixtures of CO_2 and $[C_4mim][PF_6]$ where no major change occurs in the cation-anion RDF upon addition of CO_2 to the IL. They attributed this lack of change in the structure of the IL to the strong Coulombic interactions responsible for organization in the IL.

To make the comparison shown in Figure 4.5 clearer, we calculated the coordination numbers at different concentrations in the $CS_2/[C_5mim][NTf_2]$ mixture system by inte-

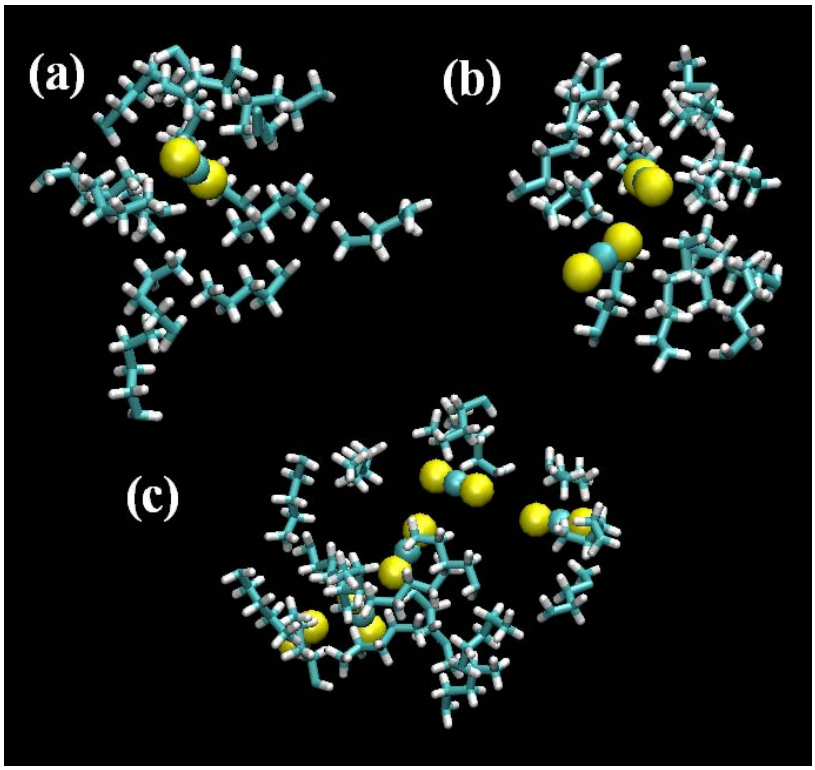

Figure 4.3. The MD snapshots of the nanostructural organization of the CS_2-tail aggregation region for (a) 5 mol %; (b) 10 mol %; (c) 20 mol % CS_2/[C_5mim][NTf_2]. (Only the CS_2 molecules and the C_5-chains are shown for clarity.)

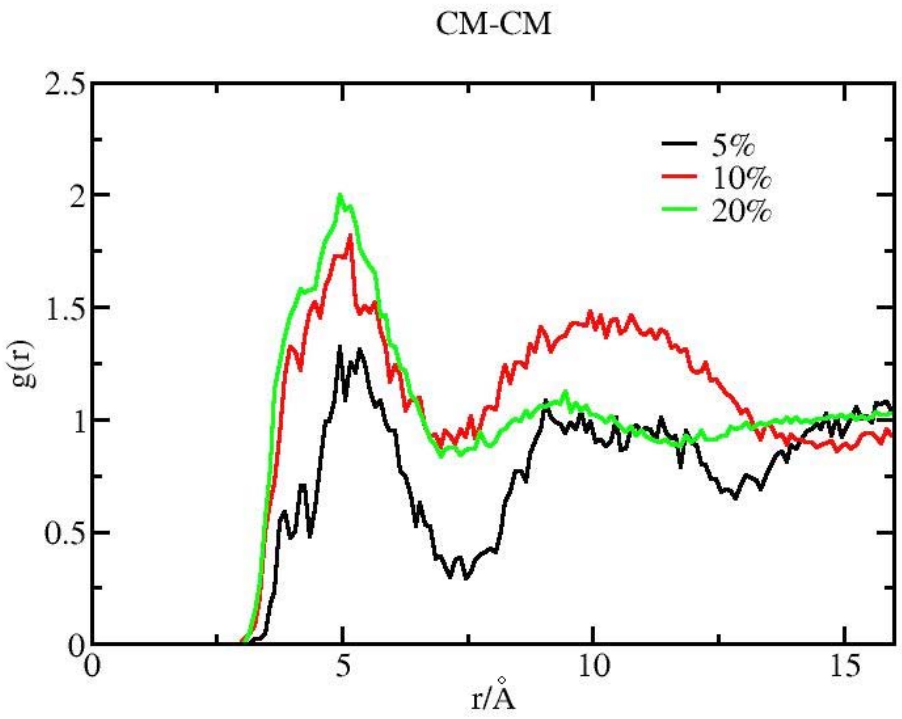

Figure 4.4. Radial distribution functions from MD simulation between a carbon atom on a CS_2 molecule and a carbon atom on a different CS_2 (CM-CM interaction) for 5, 10, and 20 mol % CS_2/[C_5mim][NTf_2].

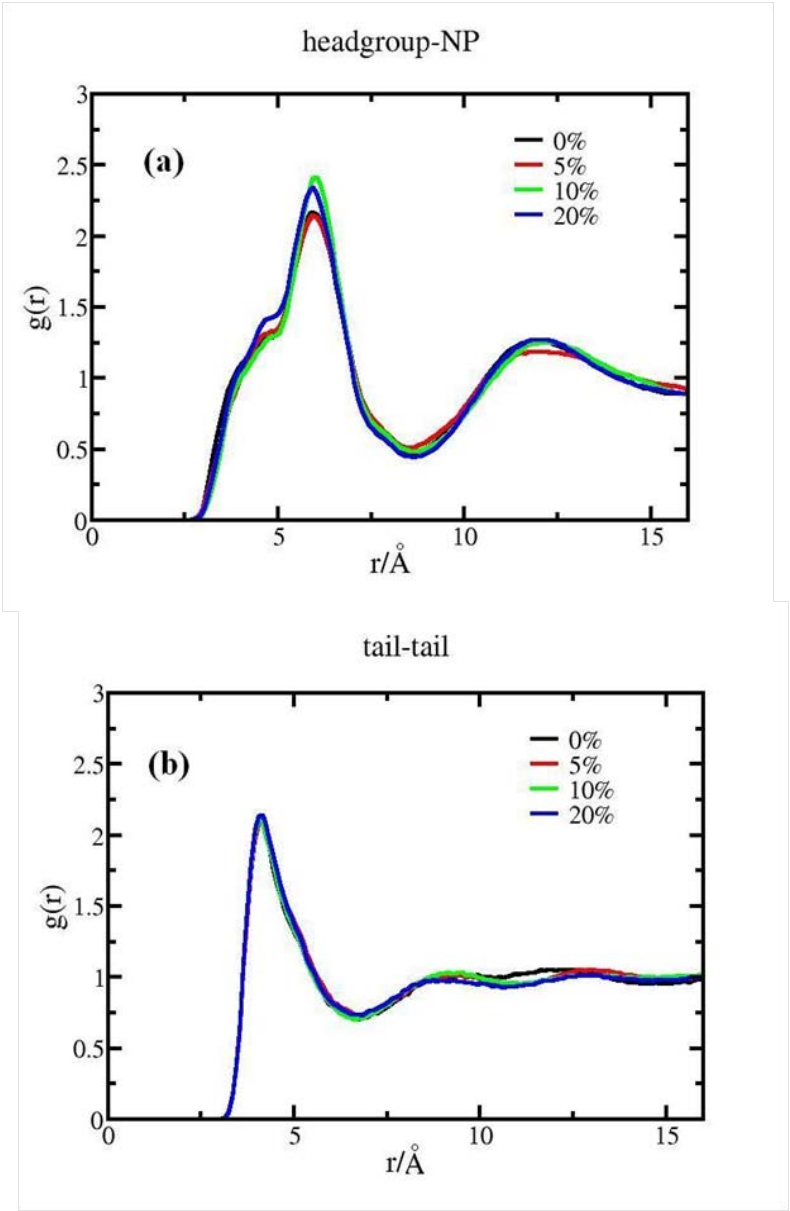

Figure 4.5. Radial distribution functions from MD simulation corresponding to cation headgroup-anion (NP) and tail-tail interactions in the CS_2/[C_5mim][NTf_2] mixture system.

grating the corresponding RDFs. Figure 4.6 shows a slight decrease in the coordination numbers associated with headgroup-NP and CT-CT interactions with increasing CS_2 mole fraction. Interestingly for 10 mol % CS_2/[C_5mim][NTf_2], there is a jump in the coordination numbers associated with headgroup-NP interactions and CM-CT interactions. A possible reason for this is that at 10 mol %, tail aggregation is slightly enhanced by the addition of CS_2 molecules.

4.4 Discussion

By making the assumption that the RSD of the IL is not affected by the addition of CS_2, Xiao et al. [31]. found that the CS_2 contribution to the RSD to be lower in frequency and narrower than the RSD of neat CS_2. Previous studies have shown that the RSD of CS_2 shifts toward lower frequency and narrows upon dilution in alkane solvents [38-42]. The origin of this dilution effect is controversial [39,43,44]. Recent experiments [42,44], however, strongly indicate that the effect is due to softening of the intermolecular potential upon dilution. For rather weakly interacting molecules, such as CS_2 and n-alkanes, one expects mixing to largely be determined by entropy. Therefore in dilute solution, a CS_2 molecule has a higher probability of interacting with an alkane molecule than with a CS_2. Because CS_2-n-alkane interactions are weaker than CS_2-CS_2 interactions, the average intermolecular potential that a CS_2 molecule sees in a dilute n-alkane solution will be weaker than in neat CS_2.

If CS_2 molecules are isolated from each other and localized in the nonpolar domains as indicated by the MD simulations, then it seems physically reasonable, based on the previous studies of CS_2 in n-alkane solvents, that the CS_2 contribution to the RSD of CS_2/IL mixtures, should be narrower than that of neat CS_2. Indeed, Xiao et al. [31] found that the CS_2 contribution to the RSD of 5 mol % CS_2/[C_5mim][NTf_2] was similar to that of 5 mol % CS_2/n-pentane. Such a comparison is justified by the fact that the CS_2 molecules are localized in nonpolar domains formed by aggregation of C_5 alkyl tails.

4.5 References

[1] A. Stark and K. R. Seddon, in Kirk-othmer encyclopedia of chemical technology, edited by A. Seidel (John Wiley & Sons, Inc., Hoboken, NJ, 2007).

[2] M. J. Earle, J. M. S. S. Esperanca, M. A. Gilea, J. N. A. C. Lopes, L. P. N. Rebelo, J. W. Magee, K. R. Seddon, and J. A. Widegren, Nature (London) **439**, 831 (2006).

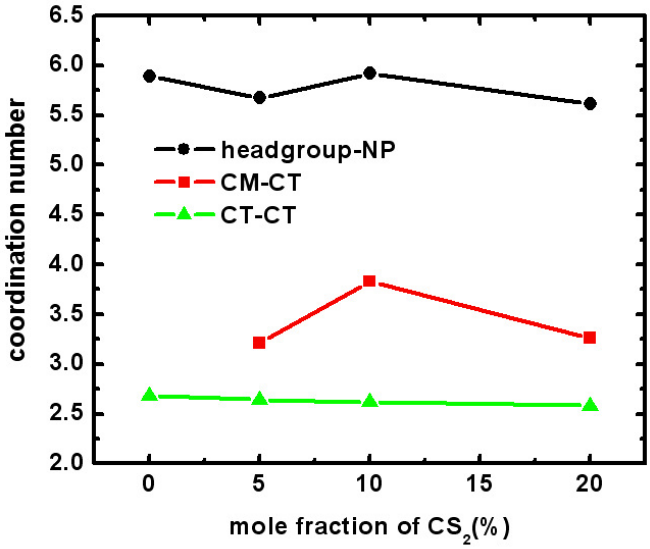

Figure 4.6. Coordination numbers obtained from integration of the MD radial distribution functions versus the mole fraction of CS_2 in $[C_5mim][NTf_2]$. Headgroup-NP – cation headgroup and the nitrogen atom on $[NTf_2]$-; CM-CT – carbon atom in CS_2 and CH_3 terminal group on the C_5-chain; CT-CT – CH_3 terminal group on the C_5-chain and CH_3 terminal group on another C_5-chain (tail-tail).

[3] Ionic liquids in synthesis, edited by P. Wasserscheid and T. Welton (Wiley VCH, Weinheim, 2007).

[4] N. V. Plechkova and K. R. Seddon, Chem. Soc. Rev. **37**, 123 (2008).

[5] M. Freemantle, Chem. Eng. News **76**, 32 (1998).

[6] N. V. Plechkova and K. R. Seddon, in Methods and reagents for green chemistry: an introduction, edited by P. Tundo, A. Perosa, and F. Zecchini (Wiley, New York, 2007). pp. 105-130.

[7] H. Weingartner, Angew. Chem. Int. Ed. **47**, 654 (2008).

[8] J. F. Wishart, J. Phys. Chem. Lett. **1**, 1629 (2010).

[9] E. W. Castner, Jr. and J. F. Wishart, J. Chem. Phys. **132**, 120901 (2010).

[10] K. R. Seddon, in The international george papatheodorou symposium: proceedings, edited by S. Boghosian, V. Dracopoulos, C. G. Kontoyannis, and G. A. Voyiatzis (Institute of Chemical Engineering and High Temperature Chemical Processes, Patras, 1999).

[11] S. M. Urahata and M. C. C. Ribeiro, J. Chem. Phys. **120**, 1855 (2004).

[12] Y. Wang and G. A. Voth, J. Am. Chem. Soc. **127**, 12192 (2005).

[13] Y. Wang and G. A. Voth, J. Phys. Chem. B **110**, 18601 (2006).

[14] J. N. A. C. Lopes and A. A. H. Padua, J. Phys. Chem. B **110**, 3330 (2006).

[15] W. Jiang, Y. Wang, and G. A. Voth, J. Phys. Chem. B **111**, 4812 (2007).

[16] Y. Wang, T. Yan, and G. A. Voth, Acc. Chem. Res. **40**, 1193 (2007).

[17] Y. Wang, W. Jiang, and G. A. Voth, in Ionic liquids IV. not just solvents anymore, edited by J. F. Brennecke, R. D. Rogers, and K. R. Seddon (American Chemical Society, Washington, DC, 2007), Vol. 975.

[18] S. Shigeto and H. Hamaguchi, Chem. Phys. Lett. **427**, 329 (2006).

[19] K. Iwata, H. Okajima, S. Saha, and H. Hamaguchi, Acc. Chem. Res. **40**, 1174 (2007).

[20] A. Triolo, O. Russina, H.-J. Bleif, and E. Di Cola, J. Phys. Chem. B **111**, 4641 (2007).

[21] A. Triolo, O. Russina, B. Fazio, R. Triolo, and E. Di Cola, Chem. Phys. Lett. **457**, 362 (2008).

[22] C. Hardacre, J. D. Holbrey, C. L. Mullan, T. G. A. Youngs, and D. T. Bowron, J. Chem. Phys. **133**, 074510 (2010).

[23] D. Xiao, L. G. Hines, Jr., S. Li, R. A. Bartsch, E. L. Quitevis, O. Russina, and A. Triolo, J. Phys. Chem. B **113**, 6426 (2009).

[24] O. Russina, M. Beiner, C. Pappas, M. Russina, T. Unruh, C. L. Mullan, C. Hardacre, and A. Triolo, J. Phys. Chem. B **113**, 8469 (2009).

[25] R. Atkin and G. G. Warr, J. Phys. Chem. B **112**, 4164 (2008).

[26] L. Gontrani, O. Russina, F. L. Celso, R. Caminiti, G. Annat, and A. Triolo, J. Phys. Chem. B **113**, 9235 (2009).

[27] M. Mizuhata, M. Maekawa, and S. Deki, ECS Transactions **3**, 89 (2007).

[28] T. L. Greaves, D. F. Kennedy, S. F. Mudie, and C. J. Drummond, J. Phys. Chem. B **114**, 10022 (2010).

[29] H. V. R. Annapureddy, H. K. Kashyap, P. M. De Biase, and C. J. Margulis, J. Phys. Chem. B **114**, 16838 (2010).

[30] A. A. H. Padua, M. F. C. Gomes, and J. N. A. C. Lopes, Acc. Chem. Res. **40**, 1087 (2007).

[31] D. Xiao, L. G. Hines, Jr., R. A. Bartsch, and E. L. Quitevis, J. Phys. Chem. B **113**, 4544 (2009).

[32] K. Fruchey and M. D. Fayer, J. Phys. Chem. B **114**, 2840 (2010).

[33] J. N. C. Lopes and A. A. H. Padua, J. Phys. Chem. B **108**, 16893 (2004).

[34] C. I. Bayly, P. Cieplak, W. Cornell, and P. A. Kollman, J. Phys. Chem. **97**, 10269 (1993).

[35] M. J. Frisch, G. W. Trucks, H. B. Schlegel et al., GAUSSIAN 03, Revision C.02, Gaussian, Inc., Wallingford, CT, 2004.

[36] W. Smith and T. R. Forester, The DL_POLY_2 user manual. (Daresbury Laboratory, Daresbury, England, 1999).

[37] C. Cadena, J. L. Anthony, J. J. Shah, T. I. Morrow, J. F. Brennecke, and E. J. Maginn, J. Am. Chem. Soc. **126**, 5300 (2004).

[38] D. McMorrow, N. Thantu, J. S. Melinger, S. K. Kim, and W. T. Lotshaw, J. Phys. Chem. **100**, 10389 (1996).

[39] T. Steffen, N. A. C. M. Meinders, and K. Duppen, J. Phys. Chem. A **102**, 4213 (1998).

[40] C. Kalpouzos, D. McMorrow, W. T. Lotshaw, and G. A. Kenney-Wallace, Chem. Phys. Lett. **150**, 138 (1988).

[41] C. Kalpouzos, D. McMorrow, W. T. Lotshaw, and G. A. Kenney-Wallace, Chem. Phys. Lett. **155**, 240 (1989).

[42] A. Scodinu and J. T. Fourkas, J. Phys. Chem. B **107**, 44 (2003).

[43] D. McMorrow, N. Thantu, V. Kleinman, J. S. Melinger, and W. T. Lotshaw, J. Phys. Chem. A **105**, 7960 (2001).

[44] Q. Zhong and J. T. Fourkas, J. Phys. Chem. B **112**, 15529 (2008).

CHAPTER 5

CONCLUSIONS

In the above three Chapters (2, 3 and 4), we have presented the MD simulations of two different systems. One is the dynamic process of graphene liquid exfoliation by using SDS/water solutions), and the other one is the microscopic structure and interactions in small solute (CS_2 or CH_3CN)/IL mixture systems. In this chapter, we will give the conclusions of these studies and discuss the possible directions for the work in the future.

5.1 Conclusion of the Study

In Chapter 2, we have studied two separation mechanisms of SDS surfactant/water + bilayer graphene mixture systems at various SDS concentrations: one is by changing the interlayer distance between graphene sheets and another one is by sliding away the relative distance between graphene sheets. By changing the interlayer distance (the separation is along the graphene-graphene VdW direction), the graphene-graphene VdW interaction is replaced by graphene-solvent interaction gradually. Because the surfactant-graphene VdW interaction is stronger than the water-graphene interaction, energy barrier in SDS/water + bilayer graphene system can be decreased by ∼0.1-0.3 eV compared with water + bilayer graphene system, but it is still not a viable separation process because of the high energy barrier (1.7 eV/nm^2). When changing the relative distance (the separation path is perpendicular to VdW direction), the energy barrier can be lowered quickly to a very small value (0.12 eV/nm^2) at certain surfactant concentrations (1.5-2.0/nm^2), which is good for exfoliation. Our results show that the sliding-away mechanism is more likely to be responsible for a liquid exfoliation process because the surfactant-graphene interaction is maximized which is critical to the separation process.

In Chapter 3 and 4, the nanostructural organizations of CH_3CN and CS_2 /[C_5mim][NTf_2] mixtures as a function of composition have been investigated by MD simulations compared to the subpicosecond intermolecular dynamics from OKE spectroscopy experiments. For CH_3CN/[C_5mim] [NTf_2] mixtures, the simulations show that CH_3CN molecules tend to be located in the interfacial regions between the ionic networks and the nonpolar domains;

moreover, the CH_3CN molecules are oriented with the negatively charged nitrogen atom pointing toward the positively charged headgroup of the cation. We see no evidence for aggregation of the CH_3CN molecules with increasing concentration, which is consistent with the complete miscibility of CH_3CN with ILs. For CS_2/[C_5mim][NTf_2] mixtures, the MD simulations demonstrate that the CS_2 molecules reside in the nonpolar domain of the ILs. In particular, the MD simulations show that for the 5 mol % mixture, CS_2 molecules are isolated from each other. With the addition of more solute molecules, aggregation of CS_2 molecules begins to occur at concentrations greater than or equal to 10 mol %. Comparison of the term for the 25 mol % mixture with the RSDs of CS_2/pentane mixtures suggests that the local concentration of CS_2 in the 25 mol % CS_2/IL mixture is higher than the bulk concentration, which would be consistent with the aggregation of CS_2 molecules in the nonpolar domains as indicated by the MD simulations.

5.2 Future Work

In conclusion, we have studied dynamics and mesoscopic structure of two different systems by using MD simulations. For the dynamic process study, it can be extended to study the liquid exfoliation of many other layered materials (e.g., MoS_2, WS_2, $MoSe_2$, $NiTe_2$, BN), such exfoliations lead to great enhancement of the surface area and change the chemical activities of the materials. Therefore, the properties of these nanosheets (in thickness) with macroscopic surface area are dramatically different from their bulk properties, and will lead to many applications in capacitor, battery, conducting filter and so on. For the structure of small solute molecule/IL mixture study, CS_2 and CH_3CN are clearly the ideal solutes to use in these studies because of their small sizes and the strength of their Kerr responses. However, there are other mixture systems that could lead to further insights into the intermolecular dynamics of solute molecules in ILs. Of particular interest are OKE measurements and MD simulations of mixtures of molecules with aromatic rings, which represents a large family of organic molecules and different interactions with ILs, and also will lead to many important applications.

APPENDIX A

OPTICAL HETERODYNE-DETECTED RAMAN-INDUCED KERR EFFECT SPECTROSCOPY

OHD-RIKES is a nonlinear optical time-domain technique that measures the collective polarizability anisotropy dynamics of a liquid. By use of a Fourier-transform-deconvolution procedure, the OHD-RIKES time-domain data can be converted to a reduced spectral density (RSD) or OKE spectrum, which is directly related to the depolarized Rayleigh/Raman spectrum of the liquid. Because of its ease of use and the fact that the resultant data are of high quality, OHD-RIKES has recently become the most common method for studying the low-frequency intermolecular modes of liquids and, in particular, ionic liquids.

A.1 Expermental Procedure

A.1.1 Preparation and Characterization of CS_2/IL Mixtures

CS2 (Aldrich, spectrochemical grade) was used without further purification. The water content of the freshly synthesized $[C_5mim][NTf_2]$ was determined by Karl Fischer titration to be <200 μg/g. The IL was kept in a nitrogen-purged glovebox or dessicator to prevent the absorption of water. Within the concentration range used in this study, 0-25 mol %, CS_2 and $[C_5mim][NTf_2]$ were completely miscible and produced optically clear mixtures. At 30 mol % and above and at room temperature, the two liquids are immiscible. Samples for the OHD-RIKES measurements were prepared by transferring an aliquot of the liquid to a 2-mm path-length, UV-grade, fused-silica sample cell (Hellma Cells) with a vacuum stopcock valve.

A.1.2 Preparation and Characterization of CH_3CN/IL mixtures

CH_3CN (Aldrich, spectrochemical grade) was used without further purification. The water content of the freshly synthesized $[C_5mim][NTf_2]$ was determined by Karl Fischer titration to be $< 200\mu$g/g. The IL was kept in a dessicator to prevent absorption of water.

Within the concentration range used in this study, 25-90 mol %, CH_3CN and $[C_5mim][NTf_2]$ were completely miscible and produced mixtures that were optically clear.

Densities of $CH_3CN/[C_5mim][NTf_2]$ mixtures were measured by use of a vibrating tube density meter (Anton Paar DMA 60 and 602) with temperature control from a recirculating bath to an accuracy of 0.1%. In the temperature range of the measurements (283-313 K), densities varied linearly with temperature.

$$\overline{V}_{mix} = x_{ACN}\overline{V}_{ACN} + (1 - x_{ACN})\overline{V}_{IL}$$

where x_{ACN} is the mole fraction of CH_3CN, and $\overline{V}_{ACN}$ and $\overline{V}_{IL}$ are the molar volumes of neat CH_3CN and $[C_5mim][NTf_2]$. The above eq. described our measured molar volumes very well. The molar volumes are additive within experimental error allows us to express the composition of the mixtures by either the mole fraction or volume fraction of CH_3CN.

A.1.3 OHD-RIKES Apparatus for CS_2/IL Mixtures

The 45-fs titanium-sapphire laser, OHD-RIKES apparatus, and method of data acquisition have been described in detail previously. To save data collection time, scans for the IL and CS_2/IL mixtures were carried out in 10 fs steps for time delays between 2 and 4 ps and in 100 fs steps for time delays between 4 and 10 ps. (Because of CS_2s shorter relaxation time, the 10 fs/100 fs step-size cutoff for CS_2 was 3 instead of 4 ps). Each OHD-RIKES signal is an average of at least 8 scans. For each sample, two data sets were obtained at heterodyne angles of $\pm 2^\circ$. The pure heterodyne signal is obtained by taking the difference of the two data sets. During an OHD-RIKES measurement, a lab-built, copper cell holder whose temperature was regulated and controlled with a thermoelectric heater/cooler system kept the sample temperature constant at 295 K.

A.1.4 OHD-RIKES Apparatus for CH_3CN/IL Mixtures

The titanium-sapphire (TiS) laser, optical delay line, and pump-probe configuration have been previously reported. Briefly, a Coherent Verdi V6 diode-pumped solid-state laser was used to pump the TiS laser, which generated 36 fs pulses as determined from the pulse-intensity background-free autocorrelation $G_0^{(2)}(t)$. To economize the data collection time, scans were performed in 50 fs steps from -2 to -0.2 ps, in 10 fs steps from -0.2 to 4 ps, and in 50 fs steps from 4 to 10 ps. Pure heterodyne signals were obtained from the difference of data sets obtained at $+5^\circ$ and -5° heterodyne angles, with each data set corresponding to an average of at least 20 scans. Samples for the OHD-RIKES measurements were held in a 2-mm path-length, UV-grade, fused-silica cell (Hellma Cells) with a vacuum stopcock valve.

During an OHD-RIKES measurement, the sample was kept at a constant temperature of 295 K using in a laboratory-built copper cell holder and thermoelectric heater/cooler system.

A.2 Analysis of OHD-RIKES Data

The reorientational dynamics of ILs are nonexponential and characterized by an intermediate power law at short times (few ps to hundreds of ps) and by a von Schweidler power and temperature dependent exponential at longer times. In the frequency domain, the longer time dynamics are associated with α- and β-relaxations and a sub-α mode lower than the α-relaxation that is thought to arise from the motion of clusters and aggregates. Since the focus of the current study is on the subpicosecond intermolecular dynamics, the form of the function used to fit the time-domain data should not matter. The time-domain signal in the $0.2 < t < 10$ ps range was therefore fit by an empirical decay function

$$r(t) = A_1 \exp(-t/\tau_1) + A_2 \exp(-t/\tau_2) + A_2 \exp(-t/\tau_3) + B \tag{2}$$

where B is a constant that accounts for other contributions to the Kerr response relaxing on a time scale much longer than the time range of the measurements. The fit of eq 2 commonly yields fast (subpicosecond) components τ_1 and τ_2 and a slow (picosecond) component τ_3 associated with reorientational relaxation. The reorientational response is modeled by an empirical impulse function

$$R(t) = [1 - \exp(-2t/\beta)][A_3 \exp(-t/\tau_3) + B] \tag{3}$$

where $\beta/2$ takes into account the inertial rise. In this study β was set equal to $(2\pi c\langle\omega\rangle)^{-1}$, where ω is the first spectral moment of the low-frequency part of the spectral density given by the equation

$$\langle\omega\rangle = \frac{\int \omega I(\omega) d\omega}{\int I(\omega) d\omega} \tag{4}$$

and where I(ω) is the spectral density and the integration is over the 0-200 cm^{-1} region. The impulse response function in eq 3 is then convoluted with the background-free pulse-intensity autocorrelation $G_0^{(2)}(t)$. After tail-matching, the convoluted reorientational response is subtracted from the OHD-RIKES signal to yield a reduced response, which contains only the electronic and vibrational contributions. The Fourier-transform-deconvolution procedure is applied to the reduced response to obtain the RSD corresponding to the subpicosecond intermolecular dynamics of the liquid. This approach to the analysis of the OKE data in the current study is the same approach used by other research groups in the analysis

of the OKE data of IL systems. Prior to performing the Fourier-transform-deconvolution procedure, a Gaussian window function is applied to the reduced response. Application of this window function, which eliminates the noise in RSD, has a negligible effect on the RSDs at high solute concentrations but causes a slight broadening of the RSDs at low solute concentrations.

A.3 Main Experimental Results

A.3.1 Intermolecular Dynamics of CS_2/IL Mixtures

With increasing CS_2 mole fraction, there is a shift to lower frequency and a narrowing of the RSDs. These spectral changes can simply be accounted for by an additivity model. Comparison of the term for the 25 mol % mixture with the RSDs of CS_2/pentane mixtures suggests that the local concentration of CS_2 in the 25 mol % CS_2/IL mixture is higher than the bulk concentration, which would be consistent with the aggregation of CS_2 molecules in the nonpolar domains as indicated by the MD simulations. If interactions of the CS_2 molecules with the polar domains also contribute to the broadening of the intermolecular vibrational spectrum of CS_2 in the mixtures, then the CS_2 contribution to the RSD should be narrower in ILs with longer alkyl side chains (i.e., C_7, C_8) due to the fact the CS_2 molecules will tend to be more deeply embedded in the interior of the nonpolar domains. Conversely, the CS_2 contribution to the RSD should be broader in ILs with short alkyl chains (i.e., C_3, C_4) because the smaller nonpolar domains will result in a greater probability of finding CS_2 molecules near the polar-nonpolar interface.

A.3.2 Intermolecular Dynamics of CH_3CN/IL Mixtures

The RSDs of the mixtures narrow and shift to lower frequency with increasing concentration of CH_3CN. Within the context of an additivity model, this behavior is mainly attributed to the increase in the contribution of the narrower and lower frequency CH_3CN component to the RSDs of the mixtures. We attribute deviations from additivity to the competition between solute-cation interactions and solute-induced disruption of the ionic networks. Using a modification of the additivity model, we showed that these deviations could be quantitatively accounted for by the intermolecular spectrum of CH_3CN in the mixture being broader and higher in frequency than the intermolecular spectrum of CH_3CN in the neat liquid.

APPENDIX B

PUBLICATIONS

1. Peng Yang, Feng Liu, "Understanding graphene production by ionic surfactant exfoliation: A molecular dynamics simulation study." *J. Appl. Phys.* **116**, 014304 (2014)

2. Edward L. Quitevis, Fehmi Bardak, Dong Xiao, Larry G. Hines Jr., Pillhun Son, Richard A. Bartsch, Peng Yang and Gregory A. Voth, in *Ionic Liquids: Science and Applications*, edited by A. E. Visser, N. J. Bridges and R. D. Rogers; ACS Symposium Series 1117(American Chemical Society, Washington, DC, 2012), Chapter **13**. pp 271-287.

3. Fehmi Bardak, Dong Xiao, Larry G. Hines, Pillhun Son, Richard A. Bartsch, Edward L. Quitevis, Peng Yang, and Gregory A. Voth. "Nanostructural organization in acetonitrile/ionic liquid mixtures: Molecular dynamics simulations and optical Kerr effect spectroscopy." *ChemPhysChem* **13**, 1687-1700 (2012).

4. Peng Yang, Gregory A. Voth, Dong Xiao, Larry G. Hines Jr., Richard A. Bartsch, and Edward L. Quitevis. "Nanostructural organization in carbon disulfide/ionic liquid mixtures: Molecular dynamics simulations and optical Kerr effect spectroscopy." *J. Chem. Phys.* **135**, 034502(1)-034502(12) (2011).